Chapter 4

APPLICATIONS

4.1 Optical Phenomena in Clouds

4.1.1 Corona

Sky under extended cloudiness looks grey with a uniform variation of transmitted light intensity. Isolated clouds look white on the background of a blue sky. This whiteness is primarily due to nonselective light scattering by water droplets in the visible. The solar light is composed of a mixture of waves having various wavelengths. A prism can divide the sunlight beam in a continuous colour spectrum. This is due to the change of the refractive index of the prism with the wavelength. Interestingly, clouds can also exhibit spectrally selective scattering if special conditions are met. In particular, coloured rings can appear in some observation directions. These phenomena are rather easily observed for thin clouds. Thick clouds are characterized by multiple light scattering, which reduces possible spectral variations of light scattered by single water droplets.

A typical example of an optical phenomenon associated with thin clouds is the corona. A corona appears as a sequence of coloured rings around a white light source observed through a cloud. These rings are most often observed at night in sunlight reflected from the Moon and passed through a thin cloud on its way to the detector or towards an observer's eye. The brightness of the background is low at night and the phenomenon is easily observed. Also the observation of the moonlight is not harmful for the human eye as compared to the direct observation of sunlight, even if seen through a thin cloud.

The corona can be fully described using the Mie theory for monodispersed droplets or polydispersions having very small coefficients of variance. Clouds with

large variations of droplet sizes produce the colourless corona, which is due to enhanced light scattering for small scattering angles. The information on the size of droplets can in principle be obtained using measurements of the angular light distribution in the corona. In particular, smaller droplets generally produce a more extended solar corona as compared to larger droplets. A simple Fraunhofer diffraction theory can be used to understand the phenomenon. It has been shown above that angular distribution of light intensity $I(\theta)$ scattered by a single spherical droplet at small angles $\theta \ll 1$ is described by the following function:

$$I(\theta) = \frac{k^2 a^2 J_1^2(z)}{\theta^2} I_0, \tag{4.1}$$

where I_0 is the intensity of incident light, J_1 is the Bessel function, a is the radius of a droplet, and $k = 2\pi/\lambda$, λ is the wavelength, and $z = ka \sin\theta \approx ka\theta$ as $\theta \to 0$. In particular, we have at $\theta = 0$:

$$I(0) = \frac{k^4 a^4}{4}, \tag{4.2}$$

where we used the following property of the Bessel function: $J_1(x) \approx x/2$ as $x \to 0$. Also we have for the dimensionless Mie intensity $i(\theta)$ in the framework of this approximation:

$$i(\theta) = x^4 \frac{J_1^2(z)}{z^2}. \tag{4.3}$$

It follows from this equation that the intensity of scattered light in the forward direction is proportional to the squared geometrical cross-section of the particle and it is inversely proportional to the fourth power of the wavelength. So incident light with a smaller wavelength produces a brighter central core as compared to incident light having a larger wavelength. The Bessel function $J_1(z)$ (and, therefore, the function $I(\theta)$) oscillates with θ. Zeros of the Bessel function $J_1(z)$ are located at z equal to 3.8317, 7.0156, 10.1735, 13.3237, and 16.4706. Therefore, at these angles dark circles in the Fraunhofer pattern are expected. We have for the angular position $\theta_{\min}$ of the first dark ring:

$$\theta_{\min} = \frac{3.8317}{ka}. \tag{4.4}$$

It follows that this angle decreases with a. However, it increases with λ. These basic rules also hold for other minima and maxima. This means that the inner part of every circle in the diffraction pattern for white light illumination conditions must be bluish as compared to the reddish colour of the outer part of each diffraction ring. The first three maxima of the diffraction pattern are located at z equal to 5.1365, 8.4163, and 11.5925, respectively. Therefore, the angular position of the

first bright ring $\theta_{\max}$ is given by

$$\theta_{\max} = \frac{5.1365}{ka} \tag{4.5}$$

or

$$\theta_{\max} = \frac{0.8175\lambda}{a}. \tag{4.6}$$

Again we see that red light maxima are shifted to outer parts of the rings.

This is actually what is observed in a corona. In particular, taking $a = 6$ μm, we obtain $\theta_{\max} = 3.1^\circ, 3.9^\circ$, and 5.5° at $\lambda = 0.4$, 0.5, and 0.7 μm, respectively. However, it should be noted that in reality angles $\theta_{\min}$ and $\theta_{\max}$ are shifted from the values given above. This is referred to as the anomalous diffraction phenomenon. The effect is explained by the fact that the Fraunhofer diffraction gives only the first coarse approximation to the reality. As a matter of fact the Mie theory should be used for an accurate simulation of the corona. Then one has a possibility to account for contributions not only by diffracted but also by reflected and refracted light beams in a given scattering direction.

We show the phase function of a spherical water droplet calculated using Mie theory at $a = 100$ μm, $\lambda = 0.5$ μm, and $n = 1.33$ in Fig. 4.1. It follows that positions of maxima and minima coincide with those calculated using the Fraunhofer diffraction theory given above. In particular, it follows from the Fraunhofer theory that that minima must be located at 0.19°, 0.35°, 0.51°, 0.67°, and 0.83°. The positions of the first three maxima are at 0.26°, 0.42°, and 0.58° for the case studied. These numbers coincide with those obtained from Mie theory (see Fig. 4.1). So both the Fraunhofer theory and the Mie theory can be used to predict the positions of minima and maxima for large spherical particles. These positions can be used for optical droplet sizing.

Note that the polarization of scattered light is low at small scattering angles.

4.1.2 Glory

Glory or anticorona appears at scattering angles close the backward direction $\theta = \pi$. The physical mechanism behind the glory occurence is the interference of backscattered rays. An approximate theory has been proposed by van de Hulst (1981). In particular, he showed that the scattered light intensity $I_{sca}(\theta)$ can be described as:

$$I_{sca}(\theta, a) = \left(c_1 J_0^2\left(ka(\pi - \theta)\right) + c_2 J_2^2\left(ka(\pi - \theta)\right)\right) x^2 I_0, \tag{4.7}$$

where constants c_1 and c_2 depend on the refractive index of particles and their size. Interestingly, the anticorona is much more robust to the change of the coefficient

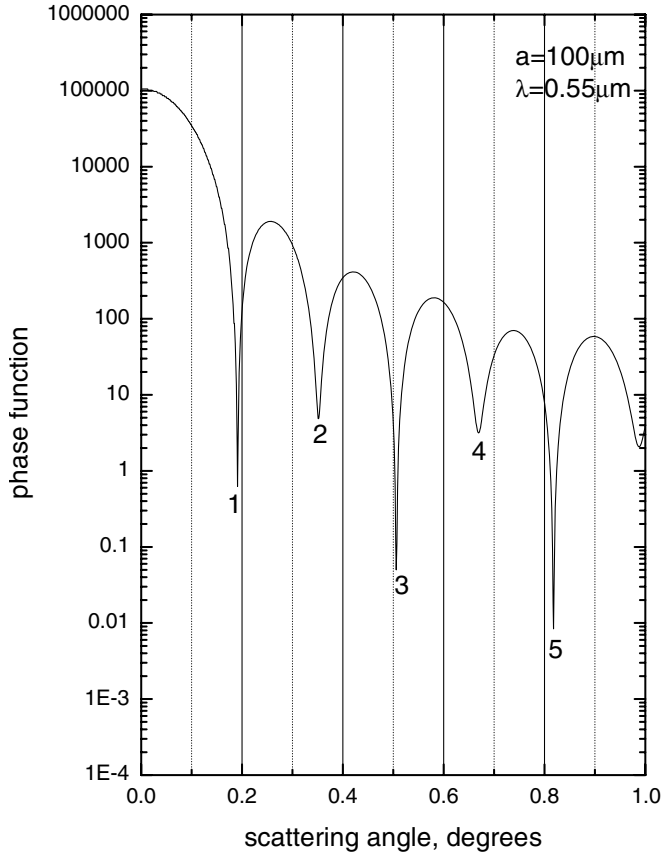

Fig. 4.1. Phase function of a water droplet having the radius 100 μm at $\lambda = 0.55$ μm. Only the small angle scattering region is shown.

of variance of the droplet size distribution as compared to the corona. In particular, it exists for relatively broad size distributions.

Let us generalize the van de Hulst's equation for the anticorona to the polydispersed case. Then it follows for the average intensity:

$$\bar{I}_{sca}(\theta) = \int_0^\infty I_{sca}(\theta, a) f(a)\, da \tag{4.8}$$

or approximately

$$\bar{I}_{sca}(\theta, a) = \left(c_1^* J_0^2\left(k\tilde{a}(\pi - \theta)\right) + c_2^* J_2^2\left(k\tilde{a}(\pi - \theta)\right)\right) I_0, \tag{4.9}$$

where we used the approximation:

$$\int_{a_1}^{a_2} \phi(\zeta) f(\zeta)\, d\zeta = f(a_3) \int_{a_1}^{a_2} \phi(\zeta)\, d\zeta, \tag{4.10}$$

with $a_3 \in [a_1, a_2]$ and

$$c_j^* = k^2 \int_0^\infty a^2 c_j(a) f(a)\, da, \quad j = 1, 2. \tag{4.11}$$

Therefore, we have for the phase function:

$$p(\theta) = p(\pi) J_0^2 \left(k a_3 (\pi - \theta)\right) + q J_2^2 \left(k a_3 (\pi - \theta)\right). \tag{4.12}$$

Parameters a_3 and q can be found fitting Eq. (4.69) with the use of Mie calculations. Also, we have used the fact that $J_0(0) = 1$, $J_2(0) = 0$. The value of a_3 is generally unknown. Let us assume that $a_3 = a_{ef}$. Then it follows:

$$p(\theta) = p(\pi) J_0^2 \left(k a_{ef} (\pi - \theta)\right) + q J_2^2 \left(k a_{ef} (\pi - \theta)\right). \tag{4.13}$$

Therefore, we might expect that the phase function must depend mostly on the scaling parameter

$$z = (\pi - \theta) k a_{ef}. \tag{4.14}$$

The dependence of the phase function on the value of z at $a_{ef} = 4(2)16$ μm and $\lambda = 0.532$ μm is shown in Fig. 4.2. Points give results according to the approximate equation given above at $q = 4.0$, $p(\pi) = 0.62$. It follows that $p(\theta)$ depends mainly on the parameter z, although there is a spread depending on the effective radius. The phase function in the exact backward direction $p(\pi)$ is almost insensitive to the value of a_{ef} and close to 0.62 at $a_{ef} = 4$ μm. There is a maximum of the phase function at $z_{\max} \approx 3$ at $a_{ef} = 16$ μm. The angular position of the maximum $\theta_{\max}$ only weakly depends on the size of particles for a given wavelength with smaller values of $z_{\max}$ for smaller particles. It follows, therefore:

$$\theta_{\max} \approx \pi - \frac{3\lambda}{2\pi a_{ef}}. \tag{4.15}$$

This means that shorter wavelengths produce larger values of $\theta_{\max}$ making the inner region of the glory ring related to the second maximum bluish. The outer parts of the ring appear reddish. This is also confirmed by the experiments and by Mie calculations (see Fig. 4.3). It follows from Fig. 4.2 that the value of the phase function in the maximum decreases with a_{ef} in the range of parameters studied. The accuracy of Eq. (4.13) decreases with z. The approximation can not be used at $z > 2.0$. However, the multiplication of the second term in Eq. (4.13) by $\nu = \exp(-0.07z)$ extends the applicability of the approximation till $z = 4$. Therefore, the approximation can be used, e.g., in conjunction with analytical results of laser sounding theory (Katsev et al., 1998).

We show the phase function $p(\theta)$ for several wavelengths at $a_{ef} = 6$ μm in Fig. 4.3. It follows from Figs. 4.2 and 4.3 that glory rings can be used for optical

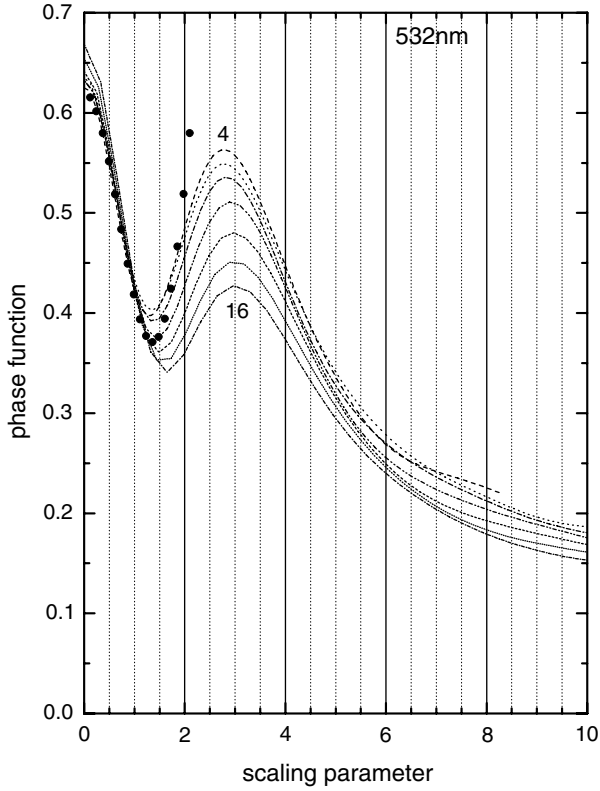

Fig. 4.2. Phase function of a water cloud at $\lambda = 532$ nm, $a_{ef} = 4$, 6, 8, 10, 12, 14, 16 μm as the function of the scaling parameter z. Points show the results using the approximate formula.

particle sizing techniques. Also we see that glory (although invisible to the human eye) exists in the infrared as well. The degree of light polarization in glory under solar light illumination conditions is shown in Fig. 4.4. It is interesting that the degree of polarization changes its sign. The neutral point, where the degree of linear polarization vanishes, depends on the wavelength. The angular position of this point θ_n is closer to the backward direction for smaller wavelengths (or larger droplets). The degree of linear polarization in the vicinity of the backward direction $\theta \approx \pi$ is positive with larger values for larger effective size parameters $x_{ef} = 2\pi a_{ef}/\lambda$ (oscillations are in predominantly in the plane perpendicular to the scattering plane). The degree of polarization is equal to zero at $\theta = \pi$. The normalized phase matrix element p_{34} shown in Fig. 4.5 describes the linear-to-circular polarization mode conversion (Kokhanovsky, 2003a). It gives the degree of circular polarization of scattered light under linearly (the azimuth 45°) polarized light illumination conditions. It follows that the circular polarization of glory for linearly

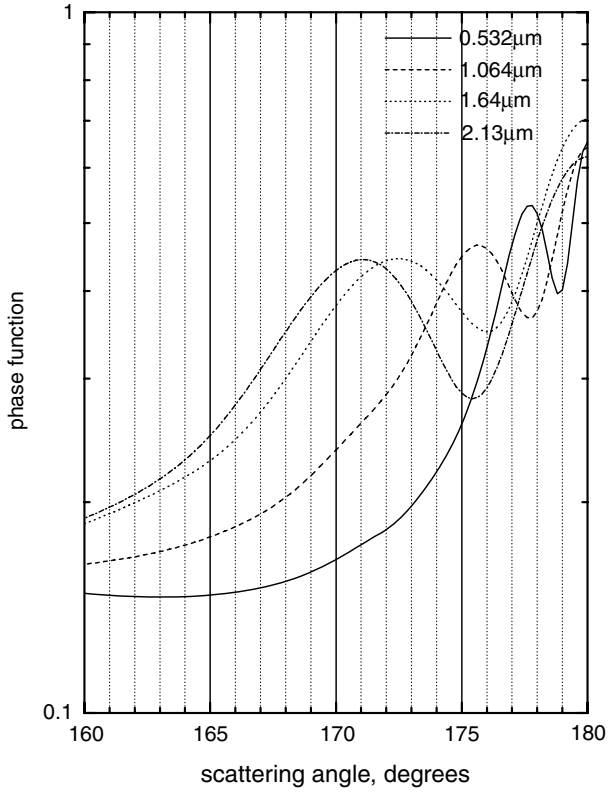

Fig. 4.3. Phase function of a water cloud at $\lambda = 0.532,\ 1.064,\ 1.64$ and 2.13 μm $a_{ef} = 6$ μm as the function of the scattering angle in the glory region.

(e.g., lidar) light illumination conditions can be quite large (especially in the infrared). The circular polarization also changes its sign in the glory region. The pulsations of circular polarization as shown in Fig. 4.5 can be used for optical particle sizing.

The normalized phase matrix element p_{44} shown in Fig. 4.6 describes the degree of circular (e.g., lidar) polarization for scattered light under circular light polarization conditions. We see that the degree of circular polarization is close to -1 for angles $\theta \to \pi$. This means that the backward scattering ($\theta \approx \pi$) does not change the absolute value of the circular polarization. However, the rotation of the electric vector is reversed. So the scattering at $\theta = \pi$ can be used in technological applications to switch the rotation direction of the electric vector. The position of the neutral point is closer to the backward scattering direction for shorter wavelengths and larger particles. This can be used for optical particle sizing using circularly polarized light beams.

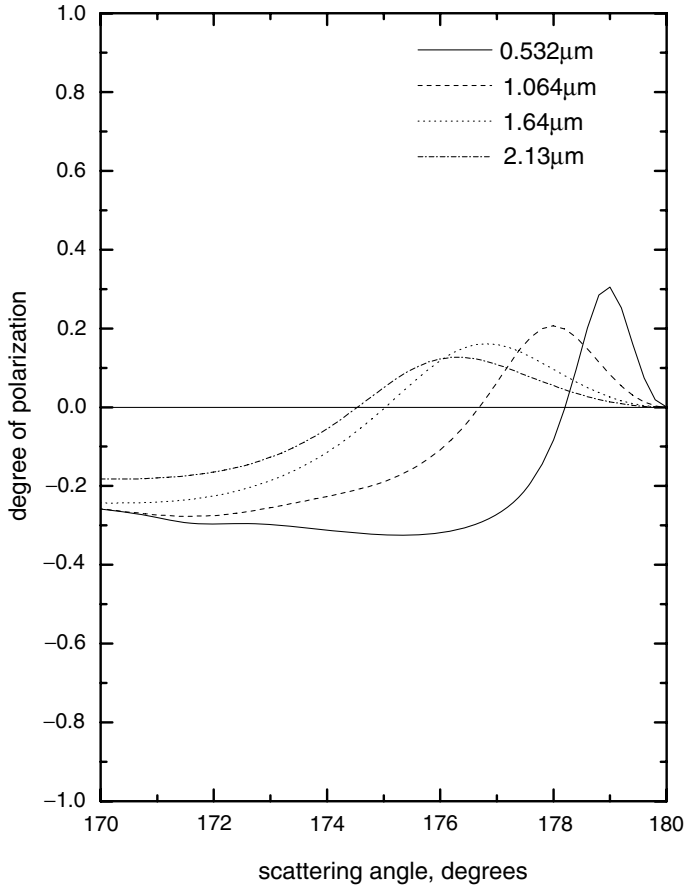

Fig. 4.4. The same as in Fig. 4.3 except for the degree of polarization.

4.1.3 Rainbow

Perhaps the best known and most familiar optical effect associated with clouds is that of the rainbow. The rainbow occurs due to the interference of rays reflected one or several times inside the droplet. Mie theory is capable to describe main features of the rainbow with a high accuracy. However, we will begin by providing some insights using the geometrical optics approximation. In particular, simple geometrical optics calculations give the following expression for the scattering angle of a singly internally reflected ray:

$$\theta_r = \pi + 2(\varphi - 2\psi), \tag{4.16}$$

where φ is the incidence angle and ψ is the refraction angle. Let us consider the

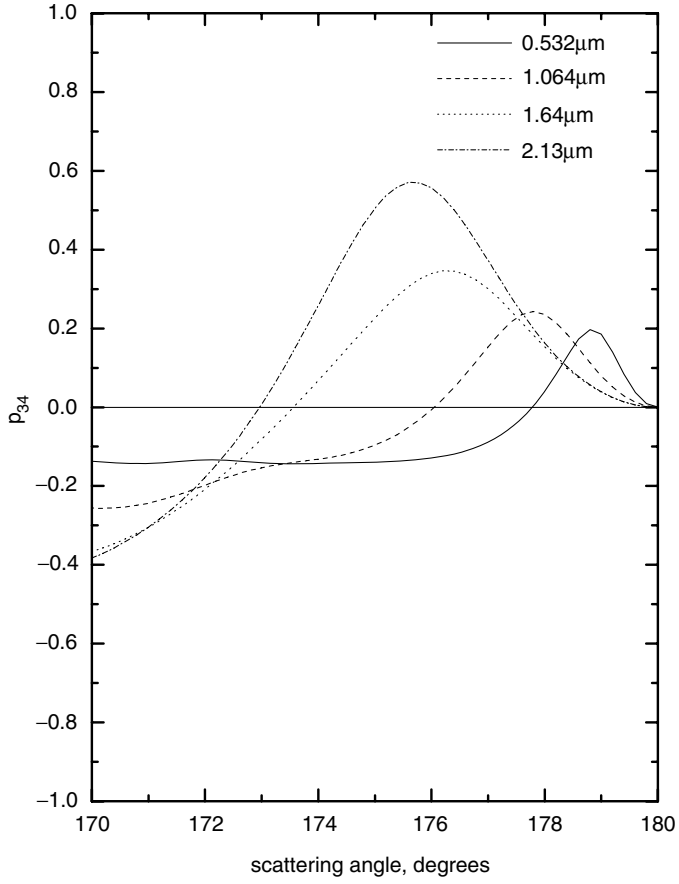

Fig. 4.5. The same as in Fig. 4.3 except for the element p_{34}.

derivative of θ_r with respect to the incidence angle. Then it follows that

$$\frac{d\theta_r}{d\varphi} = 2 - 4\frac{d\psi}{d\varphi} \tag{4.17}$$

or

$$\frac{d\theta_r}{d\varphi} = 2 - 4\frac{\cos\varphi}{n\cos\psi}, \tag{4.18}$$

where n is the refractive index and we used the Snellius law:

$$\sin\varphi = n\sin\psi. \tag{4.19}$$

It follows that θ takes a minimal value at

$$\varphi_r = \arccos\left\{\sqrt{\frac{n^2-1}{3}}\right\}. \tag{4.20}$$

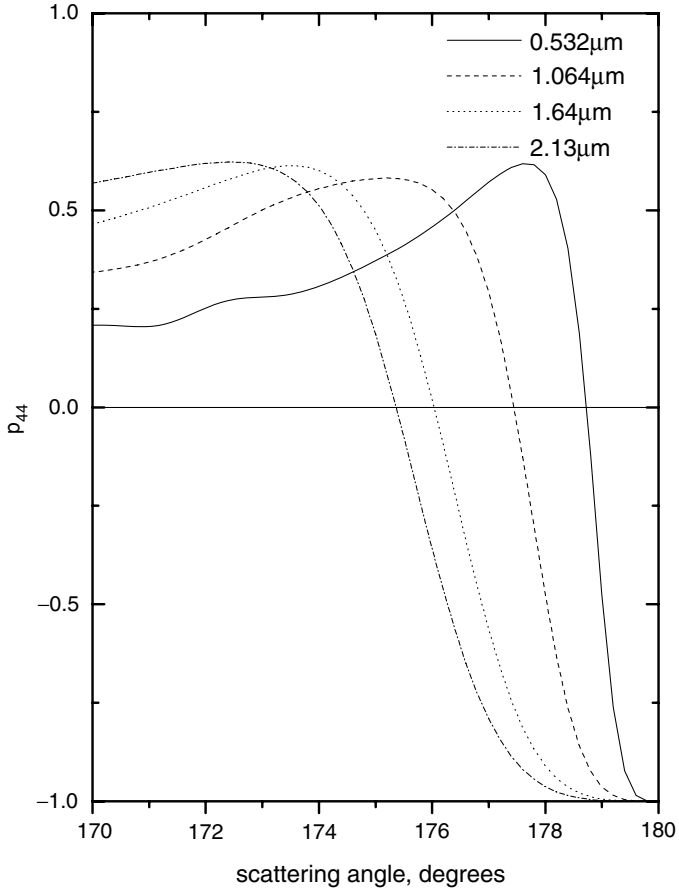

Fig. 4.6. The same as in Fig. 4.3 except for the element p_{44}.

This means that a lot of incident rays will contribute in the correspondent scattering direction. This will lead to brightening of the sky in the direction of rainbow. In particular, we have at $\lambda = 0.5$ μm and $n = 1.333$: $\varphi \approx 59^\circ$, and, therefore, $\theta_r = 139^\circ$. Therefore, to observe a rainbow, one should have a light source behind and look in the direction that makes a scattering angle of 139°.

Clearly, the same angle can be achieved for different azimuths. It will produce a characteristic feature known as the rainbow. As was noted above the angle φ depends on n, which means that both φ and θ depend on λ due to the wavelength dependence of n. In practice, this leads to the separation of colours in the rainbow. Because n slightly decreases with the wavelength for water in the visible, φ and θ decrease as well. Therefore, the outer parts of rainbow must be reddish in colour.

Quite often the secondary rainbow is observed. This rainbow originates due to double internally reflected light beams. Therefore, it is weaker in brightness than the primary rainbow. It follows for the scattering angle associated with two-times internally reflected rays:

$$\theta_r' = 2(\varphi - \psi). \tag{4.21}$$

Repeating the same procedure as above, we obtain that the derivative of this angle vanishes at

$$\varphi = \arccos\left\{\sqrt{\frac{n^2-1}{4}}\right\} \tag{4.22}$$

This gives that $\theta_r' = 129$ degrees at $n = 1.33$. Therefore, the secondary rainbow is observed at smaller scattering angles than the primary rainbow.

The accurate angular positions of maxima of light in a rainbow are given by the Mie theory. We show a characteristic rainbow pattern calculated with the Mie theory at $a_{ef} = 6$ μm and several wavelengths in Fig. 4.7. It follows that the rainbow maximum moves to smaller scattering angles for smaller wavelengths (or smaller droplets, see Fig. 4.8). This leads to the reddish colour of the outer band of a primary rainbow as observed in nature. For the secondary rainbow, the order of colors is opposite (see, e.g., http://www.philiplaven.com/index1.html).

The approximate theory of rainbow is given by Airy (1838) and Nussenzveig (1992). In particular, Airy has shown that the angular distribution of light in a rainbow at a given size parameter $x = ka$ is approximately proportional to the integral:

$$A(\theta) = \left\{\int_0^\infty \cos\left[\frac{\pi}{2}\left(by - y^3\right)\right] dy\right\}^2, \tag{4.23}$$

where

$$b = \sqrt[3]{\frac{12x^2}{\pi^2 c}}\{\theta - \theta_r\} \tag{4.24}$$

with $c = 4.89$ for the first rainbow and $c = 27.86$ for the second rainbow. Studies of this integral show that the maximum of the rainbow intensity does not coincide with θ_r but rather occurs at the somewhat larger angle $\theta_{\max}$ depending on x:

$$\theta_{\max} = \theta_r + \mathbb{C}x^{-2/3}, \tag{4.25}$$

where $\mathbb{C} = \sqrt[3]{\frac{9c\pi^2}{4}} \approx 4.77$. A similar equation, but with a different constant $\mathbb{C}$, is valid for the secondary rainbow. This dependence is confirmed by exact data shown in Fig. 4.8. It follows that the rainbow intensity at maximum increases with a_{ef}.

The thorough review of rainbow and glory theories has been conducted by Adam (2002) (see also Jackson (1999)).

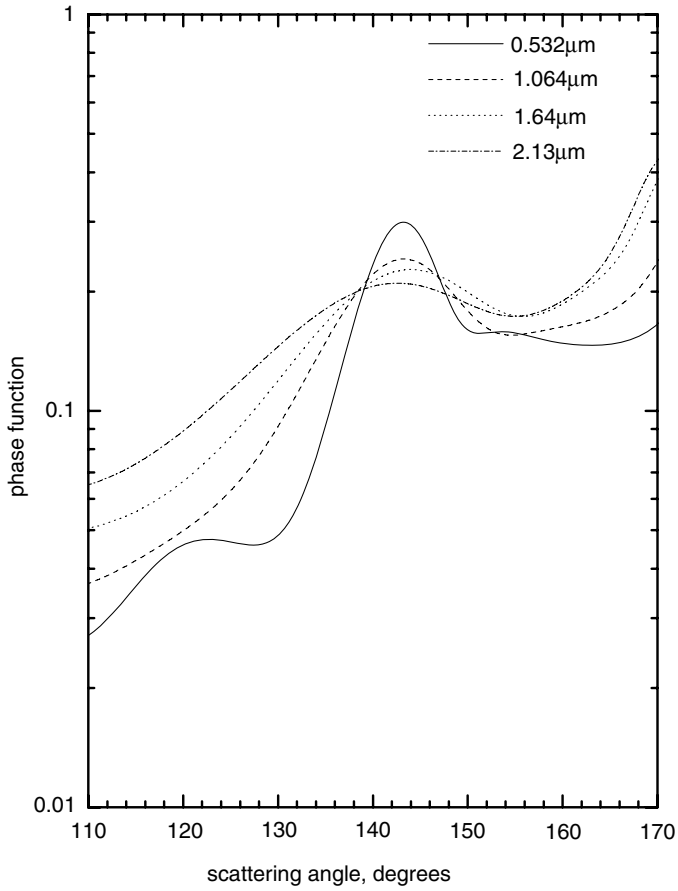

Fig. 4.7. Phase function of a water cloud at $\lambda = 0.532$, 1.064, 1.64, and 2.13μm $a_{ef} = 6$ μm as the function of the scattering angle in the rainbow region.

The degree of light polarization in a rainbow for solar light illumination conditions is quite large as shown in Fig. 4.9. It can reach 80% and even larger values depending on the size of particles and the wavelength. Oscillations occur predominantly in the plane perpendicular to the scattering plane. The reason for such a high polarization of the rainbow is due to the fact that the internal reflection of the rainbow ray in the drop occurs at the angle close to the Brewster angle equal to $\arctan(n)$.

It follows from Figs. 4.7 and 4.9 that the secondary rainbow at $\theta \approx 120^\circ$ is better visible in the degree of polarization angular pattern as compared to the intensity angular distribution. Oscillations in Fig. 4.9 at $\theta \geq 145^\circ$ are due to supernumery rainbows. They are sometimes observed in nature close to the outer band of the main rainbow.

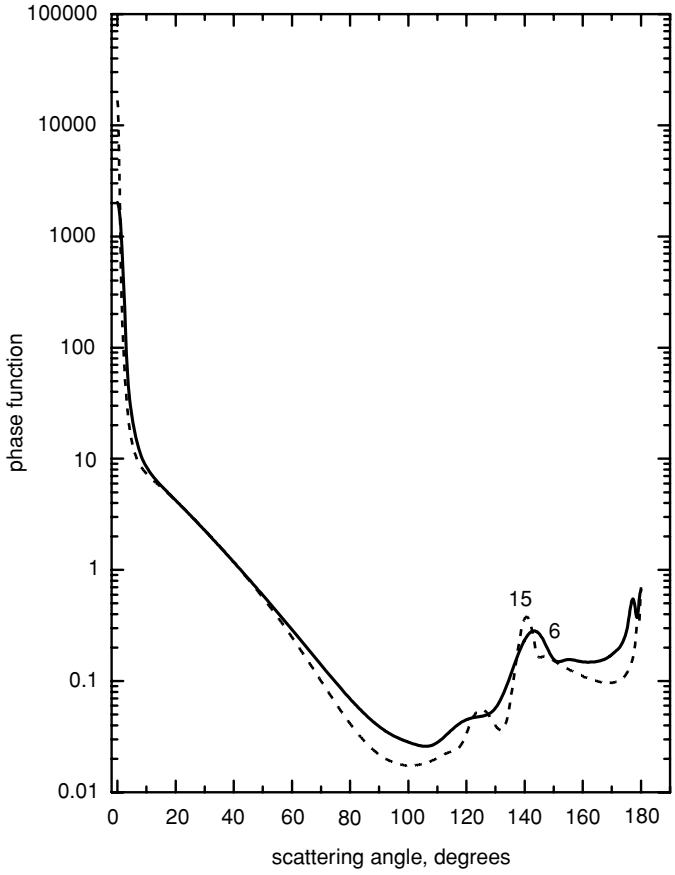

Fig. 4.8. Phase function of a water cloud at $\lambda = 0.55$ μm, $a_{ef} = 6$, 15 μm.

The wavelength dependence of the normalized phase matrix elements p_{34} and p_{44} in the vicinity of the rainbow angle is shown in Figs. 4.10 and 4.11.

4.1.4 Halo

The halo is a bright ring, which is observed around the moon or the sun. The difference from the corona is in the radius of this ring. In particular, the corona is observed for scattering angles $\theta = 0 - 5^\circ$, depending on the size of particles. The halo is observed at 22°. It should be pointed out that the Mie theory does not predict any anomaly in light scattering around 22° (see Fig. 4.8). So the halo can be explained using only the model of nonspherical particles, namely ice crystals. The most important shape of ice crystals in the terrestrial atmosphere

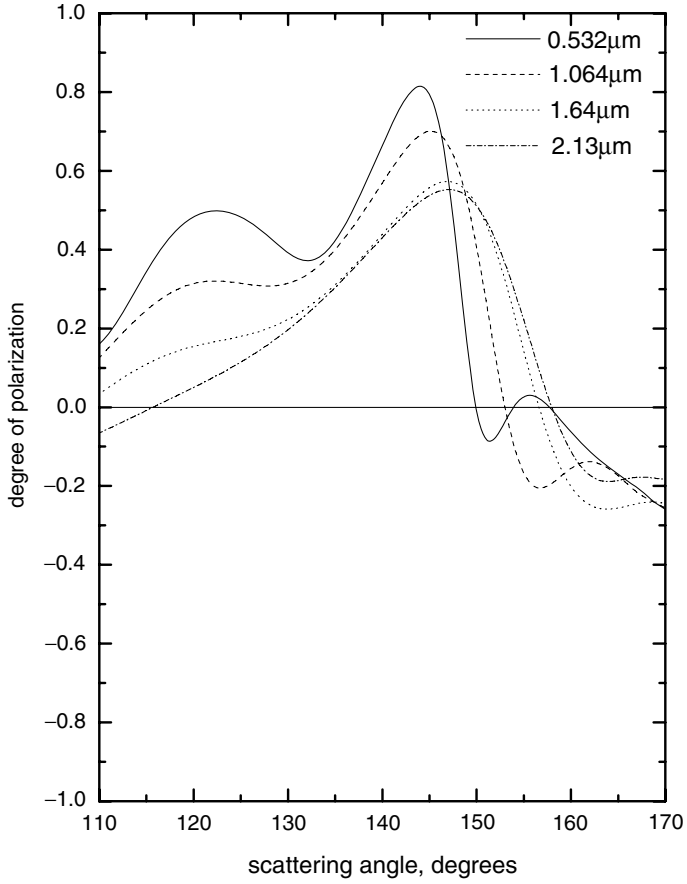

Fig. 4.9. The same as in Fig. 4.7 except for the degree of polarization.

is the hexagon. The path of a light ray in the part of crystal with the angle A is shown in Fig. 4.12. The halo corresponds to the minimal value $D_{\min}$ of the deviation angle $D = i_1 - r_1 + i_2 - r_2$. The value of D is minimal at $i_1 = i_2 \equiv i$, $r_1 = r_2 = r = \arcsin(n^{-1}\sin i)$. Here n is the refractive index. Then we have $\mathrm{A} = 2r$ (see Fig. 4.12) and $D_{\min} = 2i - \mathrm{A}$. The angle of the light beam deviation for the hexagonal prism can be obtained from the Snell's law: $n \sin r = \sin i$, where $r = \mathrm{A}/2$ and $i = (D_{\min} + \mathrm{A})/2$. This means that

$$D_{\min} = 2 \arcsin\left\{\frac{n \sin \mathrm{A}}{2}\right\} - \mathrm{A}. \tag{4.26}$$

It follows from this equation that $D_{\min} = 21^\circ 54'$ for hexagons with $\mathrm{A} = 60^\circ$ at $n = 1.31$. Also we have $D_{\min} = 45^\circ 44'$ for angles $\mathrm{A} = 90^\circ$ at $n = 1.31$. The halos associated with angles A equal to 60° and 90° are regularly observed in the

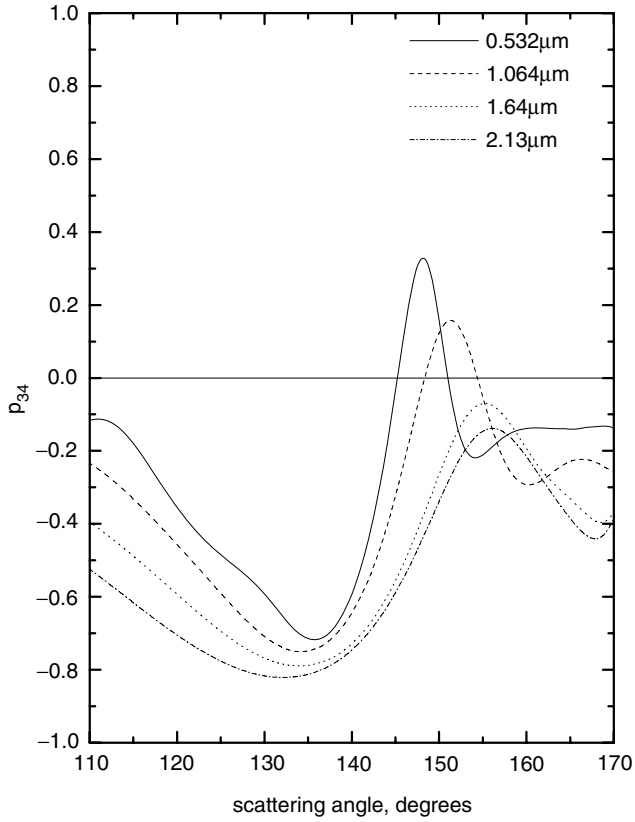

Fig. 4.10. The same as in Fig. 4.7 except for the element p_{34}.

atmosphere for randomly oriented crystals. Oriented crystals can produce the halos at other positions (Tricker, 1967). The inner part of both halos is reddish in color. This is due to the fact that $D_{\min} = 21^\circ 36'$ for red light with $n = 1.307$ and $D_{\min} = 22^\circ 22'$ for violet light with $n = 1.317$ at $\mathrm{A} = 60^\circ$. Also we have at $\mathrm{A} = 90^\circ$: $D_{\min} = 45^\circ$ for red light with $n = 1.307$ and $D_{\min} = 47^\circ 14'$ for violet light with $n = 1.317$. Therefore, it follows that the 46° halo has an angular width twice as broad. It has a smaller intensity as compared to the halo located at $\theta = 22^\circ$.

We conclude that a 46° halo develops when light enters one side of a columnar ice crystal and exits from either the top or bottom face of the crystal ($\mathrm{A} = 90^\circ$). The light is refracted twice as it passes through the ice crystal and the two refractions bend the light by 46° from its original direction. This bending produces a ring of light observed at 46° from the sun or the moon. A 22° halo develops when light enters one side of a columnar ice crystal and exits through another side ($\mathrm{A} = 60^\circ$). The light is refracted when it enters the ice crystal and once again when it leaves

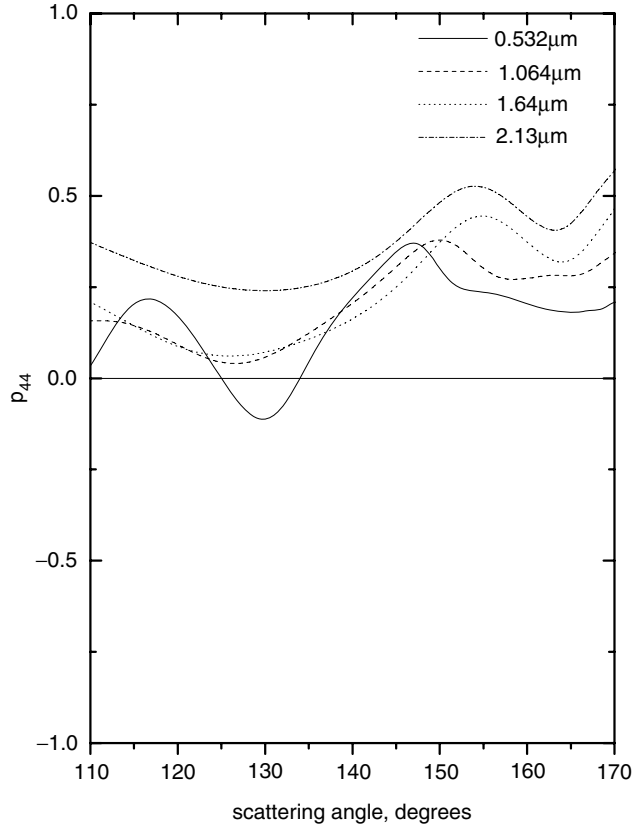

Fig. 4.11. The same as in Fig. 4.7 except for the element p_{44}.

the ice crystal. The occurrence of the 46° halo is rare (about 2% of all cases). The 22° halo is more frequent.

The halo is more easily observed for large crystals because the intensity of halos decrease with the size of crystals. A typical phase function of hexagonal ice crystals calculated using the geometrical optics approach is shown in Fig. 4.13. The halos at 22° and 46° clearly emerge from these calculations. The maximum at

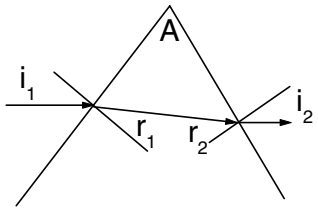

Fig. 4.12. Geometry of the problem.

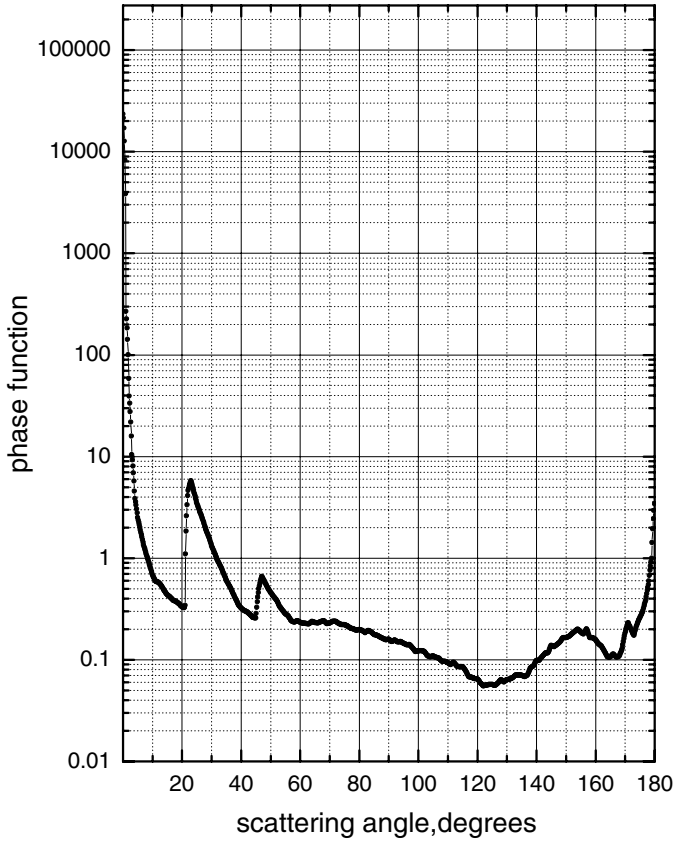

Fig. 4.13. The phase function of randomly oriented hexagonal cylinders with the effective radius 40 μm at the wavelengths 0.55 μm averaged over the size and aspect ratios distributions. The refractive index is equal to $n = 1.31$ (courtesy A. Macke).

155° is also clearly visible. The halo can be washed out by the presence of small or irregularly shaped crystals. The effects of multiple light scattering and the possible presence of supercooled water droplets also reduce the probability of halo formation. However, the halo is an atmospheric effect which occurs quite often. Some observers report a frequency of 10 times per month at certain locations.

4.2 Cloud Remote Sensing

4.2.1 Penetration Depth

The penetration depth is a parameter required in various remote sensing applications. It is defined as the length at which the intensity of incident wave is reduced

by the factor $\exp(-1)$. If the absorption coefficient of a homogeneous medium under study is known, the penetration depth can easily be estimated. It could be of value to extend this notion to random media. However, this leads to a number of problems. In particular, let us take a cloud in the sky. In this case, a strongly developed multiple light scattering occurs in the medium. The downward diffuse light intensity reaches a maximum and starts to decrease preserving the angular pattern of scattered light. Brightness of this pattern decreases as $\exp(-k\tau)$, where k is the diffusion exponent and τ is the optical depth.

Space remote sensing applications require information on the thickness of an effective layer of a cloud, which interacts with incident electromagnetic radiation. This depth can be defined as the distance ℓ at which the reflection function reaches 90% of its value for the semi-infinite layer. We can state that scattering layers positioned at depths larger than ℓ only weakly influence the signal detected by an orbiting optical instrument.

The aim of this section is to present simple analytical equations, which can be used for estimations of ℓ in a cloudy atmosphere. Generally, the equations derived can be used inside and outside gaseous absorption bands. However, in the results of the numerical calculations presented, we neglect the influence of the gaseous absorption bands on the value of the penetration depth. Generally speaking, the penetration depth can be found using results of the radiative transfer calculations similar to those presented in Fig. 4.14, where we show the dependence of the reflection function on cloud optical thickness for multiple wavelengths. Data for Fig. 4.14 were obtained using the discrete ordinate method of the radiative transfer equation solution. It was assumed that droplets are characterized by the gamma particle size distribution (PSD) with the effective radius of 6 μm and the coefficient of variance of the PSD equal to 38%. Calculations were performed at $\xi = 0.5$, $\eta = 1.0$ (nadir observation). Here ξ is the cosine of the solar angle and η is the cosine of the observation angle. Obviously, the results do not depend on the relative azimuth φ for the nadir observation conditions.

It follows from Fig. 4.14 that the penetration depth decreases with wavelength. This is mostly due to the fact that water absorption generally increases with the wavelength. In particular, we find using data shown in Fig. 4.14 that the optical penetration depth $\tau_p = \ell/s$ (with $s = 1/\sigma_{ext}$ as the photon free path in a cloud) is equal to 65.5, 37.0, 20.0, 13.2, and 5.7 for wavelengths $\lambda = 900$ nm, 1240 nm, 2250 nm, and 3700 nm, respectively.

Computations as those shown in Fig. 4.14 require a radiative transfer code. Let us show that the penetration depth can also be found using a simple analytical equation. For this we will use the exponential approximation. In particular, the reflection function $R(\xi, \eta, \varphi, \tau)$ can be presented as

$$R(\xi, \eta, \varphi, \tau) = R_\infty(\xi, \eta, \varphi) - t(\tau)\exp(-x - y)u_0(\xi)u_0(\eta), \tag{4.27}$$

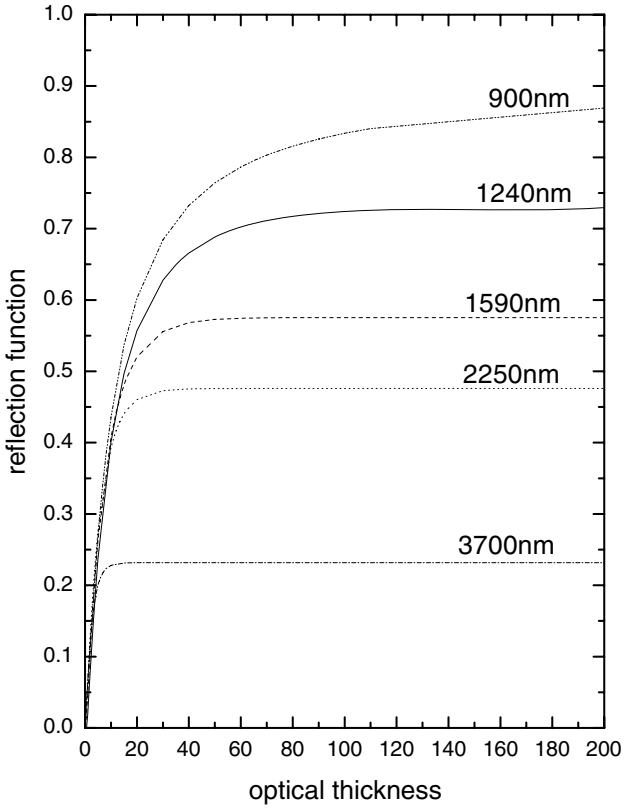

Fig. 4.14. The dependence of the reflection function on the optical thickness for several wavelengths of incident light (see details in text).

where $R_\infty(\xi, \eta, \varphi)$ is the reflection function of a semi-infinite medium having the same microphysical characteristics as a finite layer under study. The function $t(\tau)$ is the global transmittance given approximately by

$$t(\tau) = \frac{\sinh(y)}{\sinh(x + \alpha y)}. \tag{4.28}$$

Here, $x = k\tau$, $y = 4k/[3(1-g)]$, $k = \sqrt{3(1-g)(1-\omega_0)}$, $\omega_0 = 1 - \sigma_{abs}/\sigma_{ext}$, $\alpha \approx 15/14$, g is the asymmetry parameter of the phase function, σ_{abs} is the absorption coefficient and $\sigma_{ext} \equiv 1/s$ is the extinction coefficient. The accuracy of Eq. (4.27) has been thoroughly studied above.

It follows from Eq. (4.27) at $\tau = \tau_p$:

$$ut(\tau_p)\exp(-x(\tau_p) - y(1-u^*)) = b, \tag{4.29}$$

where $b = 0.1$. We used the following approximate result for the reflection function of a semi-infinite weakly absorbing medium:

$$R_\infty(\xi, \eta, \varphi) = R_{0\infty}(\xi, \eta, \varphi) \exp(-\mathbb{C}y), \tag{4.30}$$

where $R_{0\infty}(\xi, \eta, \varphi)$ is the reflection function of a semi-infinite medium, under the assumption that absorption of radiation in a cloud does not take place and

$$\mathbb{C} = (1 - 0.05y)\mathbb{N}, \tag{4.31}$$

$$\mathbb{N} = \frac{u_0(\xi)u_0(\eta)}{R_{0\infty}(\xi, \eta, \varphi, \tau)}. \tag{4.32}$$

Equation (4.30) is accurate to within 5% at $y \leq 1.7$. After simple algebraic derivations, it follows from Eq. (4.29):

$$\tau_p = \frac{1}{2k} \ln \{2p\mathbb{N} \sinh(y) \exp[-(1 - \mathbb{C})y] + \exp(-\alpha y)\} - \frac{2\alpha}{3(1 - g)}, \tag{4.33}$$

where $p = 1/b$. We have from Eq. (4.33) at $k = 0$ taking a limit:

$$\tau_p = \frac{4(p\mathbb{N} - \alpha)}{3(1 - g)}. \tag{4.34}$$

Equation (4.33) gives the result that we intended to gain from the very beginning. The dependence $\tau_p(\lambda)$ for a water cloud having the same microphysical characteristics and observation conditions as those used in Fig. 4.14 are shown in Fig. 4.15. The Mie theory was used to calculate ω_0, $\sigma_{ext} = 1/s$, and g in Eq. (4.33). The gaseous absorption was neglected. Symbols correspond to values of τ_p obtained from the data given in Fig. 4.14. We see that our approximate equation can be used for an accurate estimation of the sunlight penetration in clouds. Note that values obtained for $\tau < 10$ may be biased as the accuracy of Eq. (4.27) decreases in these cases. However, we do not restrict this plot to values below 2 μm to show the general trend of $\tau_p(\lambda)$. Furthermore, the point at 3.7 μm indicates that Eq. (4.33) might even be used at $\tau_p \in [5, 10]$. The following approximate result for the function $R_{0\infty}(1, \xi)$ was used in the calculations presented in Fig. 4.14:

$$R_{0\infty}(1, \xi) = \frac{0.37 + 1.94\xi}{1 + \xi}. \tag{4.35}$$

This equation is accurate to within 5% for the nadir observation and most solar incident angles used for cloud remote sensing (oblique incident angles are excluded).

Figure 4.14 quantifies the result already mentioned above. Namely, the optical penetration depth generally decreases with the wavelength. However, at some narrow spectral intervals, the opposite is true (see, e.g., the region close to 1 μm in Fig. 4.15). The value of τ_p changes from approximately 100 at $\lambda = 0.5$ μm

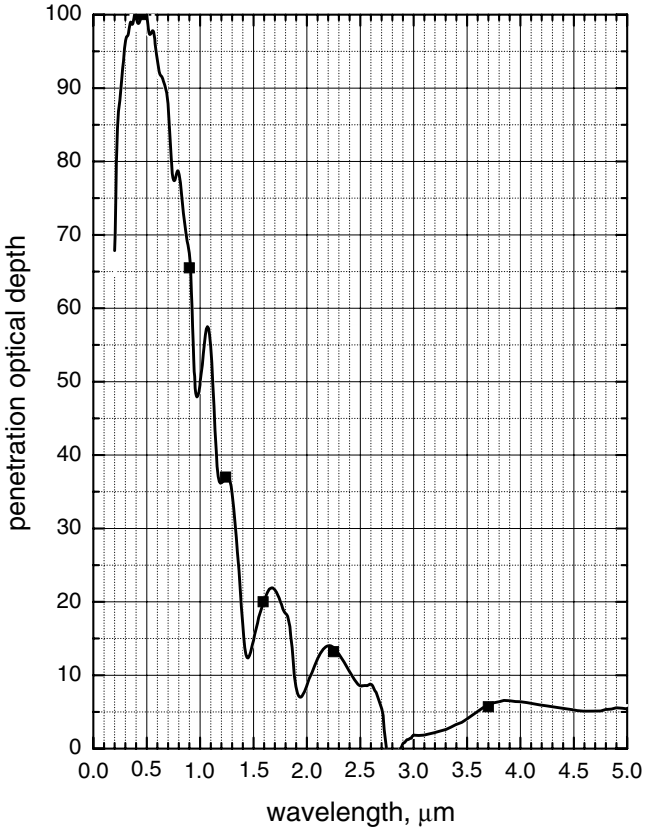

Fig. 4.15. The dependence of the penetration optical thickness on the wavelength obtained using the approximate equation for water droplets having the effective size 6 μm at the nadir observation and the solar angle equal to 60°. Symbols give the results obtained using the numerical solution of the integro-differential radiative transfer equation.

to approximately 6 at $\lambda = 3.7$ μm for the typical case shown in Fig. 4.15. Using a typical value of $\sigma_{ext} = 50$ km^{-1}, we obtain that the value of ℓ changes from 120 m at $\lambda = 3.7$ μm to 2000 m at $\lambda = 0.5$ μm. In fact, Fig. 4.15 is also applicable to ℓ after the rescaling the ordinate. For example, the ordinate should be multiplied by 10 at $\sigma_{ext} = 100$ km^{-1}. Then ℓ is given in meters.

It follows from Fig. 4.15 that the radiance detected at different wavelengths originates in part from different cloud depths. This sets an important question as far as cloud satellite remote sensing is concerned. Namely, the cloud liquid water path (LWP) and the effective radius of droplets are usually obtained from measurements of reflectances at multiple wavelengths. This does not lead to complications for homogeneous clouds. However, homogeneous clouds do not exist.

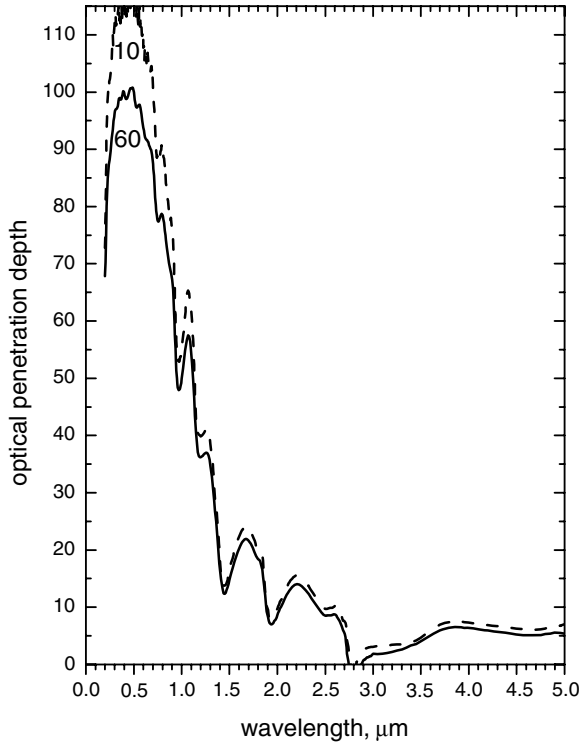

Fig. 4.16. The same as in Fig. 4.15 except the results for the solar angle 10° are also shown.

For example, the size of droplets usually increases from the bottom to the top of a cloud layer. It means that the radius of droplets obtained at 3.7μm (a_{ef}(3.7 μm)) is not necessarily representative for a whole cloud. In this case, the derivation of the LWP as the product of the optical thickness in the visible and a_{ef}(3.7 μm)(we omit a numerical multiplier) may bias the derived LWP considerably. Therefore, it is of importance to specify the wavelengths used to derive a_{ef} and the LWP while referring to their values obtained from the optical instruments onboard satellites. Generally, decreasing the wavelength will lead to smaller values of a derived a_{ef} (and also smaller values of the LWP).

It follows from Fig. 4.16 that the value of τ_p is larger for the illumination closer to the normal. This can be explained by the fact that photons injected into the absorbing turbid medium along oblique angles escape easier and do not penetrate as deeply as photons incident on a given medium along the normal.

The spectral dependence of the optical penetration thickness is shown in Fig. 4.17 for various sizes of particles. We see that the value of τ_p decreases with the size of particles in the infrared. This can be expected from the greater light absorption by larger droplets. We also found that the optical penetration depth is slightly larger for larger droplets in the visible. This is due to larger values of g for

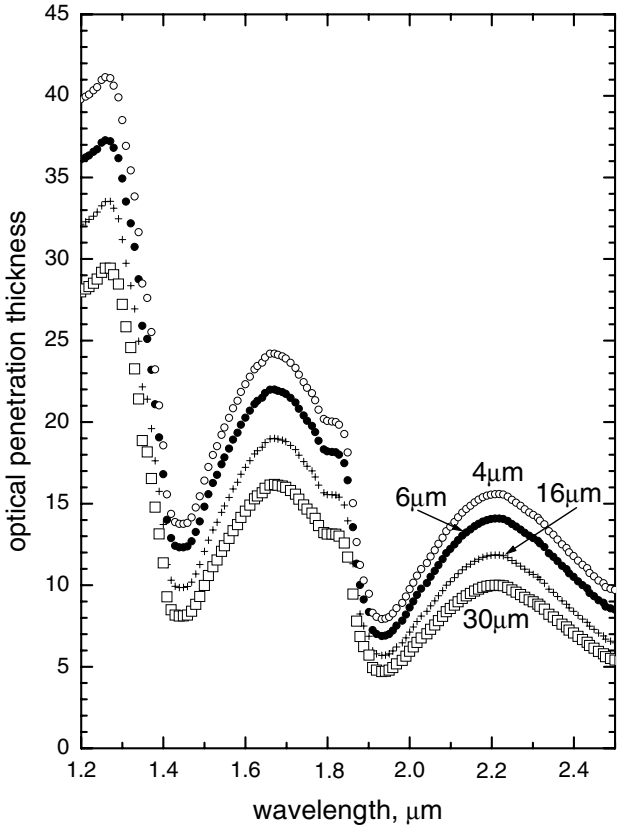

Fig. 4.17. The same as in Fig. 4.15 except the results for the several values of the effective droplet radius are shown.

clouds with larger droplets. The account for the gaseous absorption will modify the data shown in Fig. 4.16, adding an oscillating part on the general background curve depending on the gas type/concentration. However, we do not consider this contribution in any detail here.

Equation (4.33) becomes less accurate for values of the single scattering albedo (SSA) smaller than 0.95. This case may be of importance for polluted clouds and also for ice clouds having large crystals and, therefore, increased value of light absorption. In this case, the problem can be solved using the general asymptotic equation valid for cloud optical thicknesses larger than 10 and an arbitrary SSA. This equation has the following form (Nakajima and King, 1992):

$$R(\xi, \eta, \varphi, \tau) = R_\infty(\xi, \eta, \varphi)\left[1 - ml\bar{\mathbb{N}}(\xi, \eta, \varphi, \tau)\left(1 - l^2\exp(-z)\right)^{-1}\exp(-z)\right], \tag{4.36}$$

where $\bar{\mathbb{N}}(\xi, \eta, \varphi) = u(\xi)u(\eta)/R_\infty(\xi, \eta, \varphi)$, $z = 2k\tau$, and, therefore,

$$\tau_p = (2k)^{-1} \ln \left(ap + l^2\right), \tag{4.37}$$

where

$$a = \frac{mlu(\xi)u(\eta)}{R_\infty(\xi, \eta, \varphi)}. \tag{4.38}$$

The issues related to the numerical calculation of asymptotic parameters and functions k, l, m, $u(\xi)$ and $R_\infty(\xi, \eta, \varphi)$ are discussed by Nakajima and King (1992). However, note that the essential simplicity characteristic to Eq. (4.33) is lost then.

Equation (4.27) follows from Eq. (4.36), assuming that $l = \exp(-\alpha y)$,

$$mu(\xi)u(\eta) = (1 - \exp(-2y))\, u_0(\xi)u_0(\eta) \tag{4.39}$$

as shown above. The same correspondence exists between Eqs. (4.37) and (4.33) (with account for Eq. (4.30)).

4.2.2 Cloud Optical Thickness

4.2.2.1 Retrieval procedure

Equations presented in Chapter 3 can be used for rapid estimations of the radiative and polarization characteristics of cloudy media. They can also be used to check the accuracy of new algorithms, using the fact that the numerical solution of the radiative transfer equation, and the results presented above for optically thick layers should converge as $\tau \to \infty$ and $\beta \to 0$.

The most important area of application of approximate solutions lies in the field of remote sensing (King, 1981, 1987; Kokhanovsky, 2000; Kokhanovsky, 2001; Kokhanovsky and Zege, 1996; Kokhanovsky et al., 2003; Rozenberg, 1967; Rozenberg et al., 1978). In particular, the usage of asymptotic equations (valid as $\tau_0 \to \infty$) allows us to avoid the compilation of so-called look-up tables (LUTs) in the case of optically thick clouds and, therefore, to speed up the retrieval process. Currently, LUTs are widely used in passive cloud remote sensing (Arking and Childs, 1985; Nakajima and King, 1990; Rossow et al., 1989). The minimization of differences between measured and stored (e.g., in LUTs) spectral reflectances is used as a main tool to derive cloud optical and microphysical characteristics.

The reflection function of a cloud over a reflective surface with the Lambertian albedo A can be presented as

$$R = R_b + \frac{At^2 u_0(\xi)\, u_0(\eta)}{1 - Ar}, \tag{4.40a}$$

with

$$R_b = R_{0\infty} - t u_0(\xi)\, u_0(\eta) \tag{4.40b}$$

in the visible. Here,

$$t = \frac{1}{\alpha + 0.75\tau^*} \tag{4.40c}$$

is the global transmittance with $\alpha \approx 1.07$ and $\tau^* = \tau(1 - g)$.

We have for the global transmittance in the visible from Eq. (4.40a) after simple algebraic calculations:

$$t = \frac{(1 - rA)\,\Pi}{1 - rA(1 + \Pi)}, \tag{4.41a}$$

where the function Π is introduced. It is given by

$$\Pi \equiv \Pi(\eta, \xi, \varphi) = \frac{R_{0\infty}(\eta, \xi, \varphi) - \hat{R}_{mes}(\eta, \xi, \varphi, \tau)}{u_0(\eta) u_0(\xi)}. \tag{4.41b}$$

The analytical results for functions $R_{0\infty}(\eta, \xi, \varphi)$ and $u_0(\eta)$ have been presented above. Thus, the global transmittance t, and correspondingly the total reflectance or the spherical albedo $r = 1 - t$, can be obtained from Eqs. (4.40) and (4.41) and knowledge of the surface albedo A and the measured value of the reflection function $\hat{R}_{mes}(\eta, \xi, \varphi, \tau)$.

For such a retrieval it is not necessary to know the optical thickness of clouds and the average size of droplets. This is an extremely important point for climate studies, where the global and temporally averaged value of the cloud spherical albedo $r = 1 - t$ is an important parameter. Usually $r < 0.8$ for natural water clouds in the visible (Danielson et al., 1969), which implies that clouds with optical thicknesses larger than 70–100 appear not very often (Trishchenko et al., 2001). The reduced reflectance in the visible can be also related to aerosol absorption in clouds (Melnikova and Mikhailov, 1994, 2000) and to the inhomogeneity and finite size of clouds (Stephens and Tsay, 1990).

Using Eq. (4.40), we obtain $t \equiv \Pi$ at $A = 0$, and $t = 0$ ($r = 1$) at $A = 1$. This shows that all photons incident on optically thick nonabsorbing clouds over surfaces with $A = 1$ survive and return back to outer space. They yield no information about actual cloud thickness. This explains why the retrieval of cloud parameters over bright surfaces (e.g., snow and ice) can be hardly performed in the visible (Platnick et al., 2001).

The information on the global transmittance t can be used to find the scaled optical thickness (King, 1987; Rozenberg et al., 1978), given by

$$\tau^* = \tau(1 - g). \tag{4.42}$$

It follows from Eq. (4.40c):

$$\tau^* = \frac{4}{3}\left[t^{-1} - \alpha\right], \tag{4.43}$$

where t is given by Eq. (4.40). The value of τ^* can be obtained even in the absence of information about the size of droplets and the actual optical thickness of clouds.

Equation (4.43) can be used for the retrieval of τ^* from the measurement of the reflection function at a single wavelength (King, 1987). Equation (4.42) is used for the derivation of the optical thickness τ if the value of g is known (Rossow, 1989) (approximately 0.74 for ice clouds as previously discussed). However, for warm clouds the asymmetry parameter g depends on the size of droplets even for nonabsorbing channels. Often the dependence $g(a_{ef})$ is neglected and it is assumed that $a_{ef} = 10$ μm for water clouds (Rossow and Schiffer, 1999). Then it follows from that $g = 0.86$ at $\lambda = 0.65$ μm and $a_{ef} = 10$ μm. This value of g can be used for a crude estimation of the optical thickness of liquid clouds.

Errors can be introduced if one assumes the fixed *a priori* defined value of g. It follows at $\lambda = 0.65$ μm that $g = 0.84$–0.87 at $a_{ef} = 4$–20 μm. From Eq. (4.42), we have $\tau = \Im\tau^*$, $\Im \equiv (1-g)^{-1} \approx 6.3$–$7.6$ and $\tau \in [9.4, 11.5]$ at $\tau^* = 1.5$, depending on the value of g used. The assumption that $a_{ef} = 10$ μm yields $g = 0.86$ and $\Im = 7.2$, $\tau = 10.7$. This leads to a relative error of 7–14% in the retrieved optical thickness (i.e., a range of possible values from $\tau = 9.4$ to $\tau = 11.5$ instead of $\tau = 10.7$). This uncertainty in the optical thickness can be removed if measurements in the near infrared region of the electromagnetic spectrum are performed, enabling the size of droplets and, therefore, the asymmetry parameter g estimation. For this, however, we should be sure that we have a liquid and not an ice or a mixed phase cloud. Another uncertainty arises due to the possible contamination of clouds by absorbing aerosols (Asano et al., 2001, 2002). Then Eq. (4.40) is not valid and we must account for the fact that the cloud single scattering albedo (SSA) differs from one.

4.2.2.2 Hurricane Erin

Let us consider optical thickness retrieval for the Hurricane Erin, located in the western Atlantic (39.3 N, 60.4 W) on September 13th, 2001 (16:21 UTC). By definition, hurricanes contain winds in excess of 119 km per hour and large areas of heavy rainfall. Therefore, they belong to the most dangerous natural hazards. This explains the great interest in hurricane research especially in recent years (Simpson, 2002). Physical characteristics of hurricanes are usually obtained using radar remote sensing techniques (Heymsfield et al., 2001). The optical imagery

serves as an important tool for a timely identification of hurricanes and for tracking their trajectories (especially where radar is not available). The optical remote sensing techniques can also be used to study physical characteristics of hurricanes like hurricane-top height, the LWP, the thermodynamic phase of particles and their size. The enhanced spatial resolution of optical imagery allows for important complimentary information as compared to microwave techniques. Clearly, some additional difficulties and problems can arise in this case. They are related mostly to the relative importance of three-dimensional (3-D) effects (e.g., in a hurricane wall), scattering by nonspherical particles, and large values of the geometrical and optical thickness of hurricanes.

Erin can be traced back to a tropical wave that emerged from Western Africa on August 30th, 2001. The hurricane took a long journey from the coast of Africa to the northern Leeward Islands and then to Greenland over the western Atlantic before it merged with high-latitude cyclonic flow on September 17th, 2001. Note that this hurricane was the first one for which a comprehensive 3-D image of the complete inner core (including the eyewall and the eye) has been created.

The retrieval procedure is performed using the SeaWiFS local area coverage imagery with the spatial resolution of about 1×1 km, taken on September 13th, 2001. The SeaWiFS instrument measures the top-of-atmosphere backscattered light intensity in eight channels (412, 443, 490, 510, 555, 670, 765, and 865 nm). Only data for the wavelength 412 nm are used in this study. This is due to a low spectral variation of the hurricane reflectance, which is due to large size of particles (as compared to the light wavelength) in a hurricane.

The map of retrieved values of transport optical thickness is given in Fig. 4.18. We see that the value of the transport optical thickness is mostly in the range of 4–10 for the hurricane studied.

We also have selected a core of a hurricane and made the retrieval of the transport optical thickness for this special case. The map obtained is shown in Fig. 4.19. The statistical distribution of the transport optical thickness for this case is given in Fig. 4.20.

One can find black areas surrounded by white color in Fig. 4.19. They correspond to negative values of the reduced optical thickness obtained owing to possible influence of 3-D effects as discussed above (e.g., shadowing effects). To determine the hurricane optical thickness, the value of the asymmetry parameter should be known. The value of g is around 0.85 for water clouds and it is close to 0.75 for ice clouds. The retrieved cloud optical thickness distribution, assuming the value of $g = 0.85$, coincides with that given in Figs. 4.18–4.20 (but scaled using the factor $B = 1/(1- g)$). Note that we have at $g = 0.85$, $B \approx 6.7$. Therefore, the spatial distribution of τ for the case given in Fig. 4.18 has a main maximum at cloud

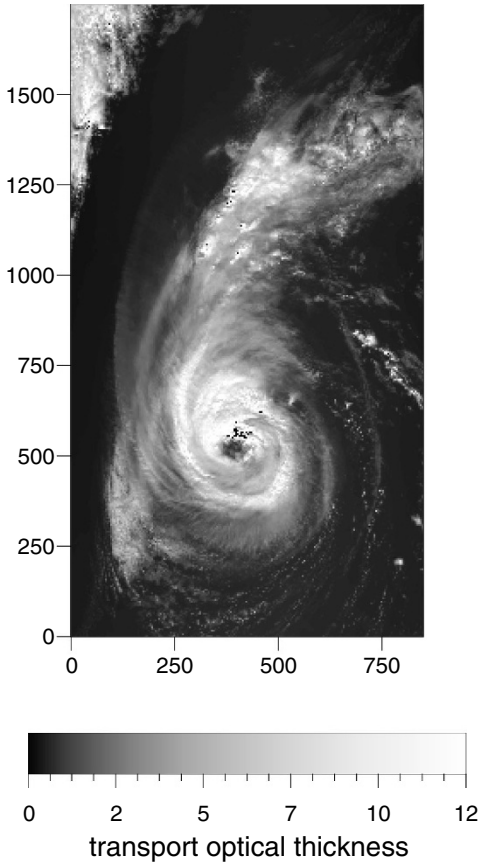

Fig. 4.18. The transport optical thickness map.

optical thickness equal to 35. Note that results at small and large values of cloud optical thickness can be biased because the accuracy of our technique decreases there. However, it works well for values of optical thickness in the range of 10–100, which are characteristic numbers for most pixels with a hurricane. We also found a highly nonuniform distribution of cloud optical thickness in the hurricane eye. The mode optical thickness was found to be equal seven in the hurricane eye.

The hurricane spherical albedo map and frequency distribution are given in Figs.4.21a and 4.21b. We see that most frequent value of a hurricane albedo is around 0.86. The distribution of the spherical albedo is similar to the well-known beta distribution, having abrupt decrease at r close to 1.0. Large values of r for a hurricane suggest that hurricanes can potentially modify planetary albedo (at least during the hurricane season). This can be also enhanced by foam-covered rough seas, which are produced by hurricanes.

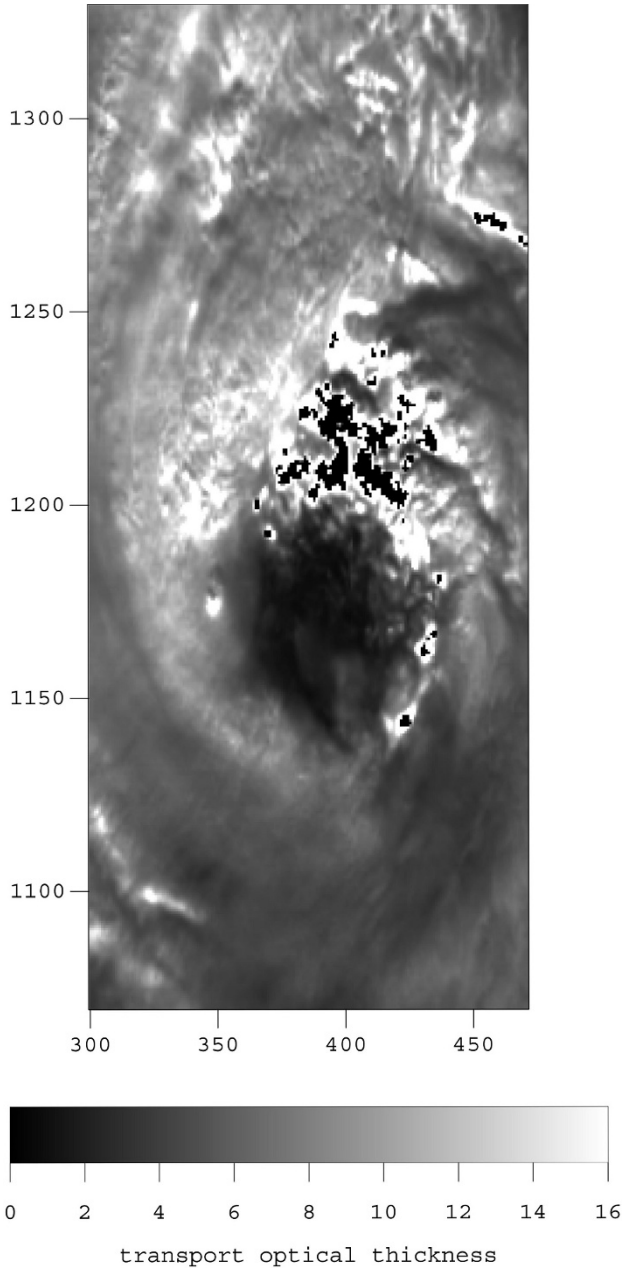

Fig. 4.19. The same as in Fig. 4.18 but for the region close to the hurricane eye.

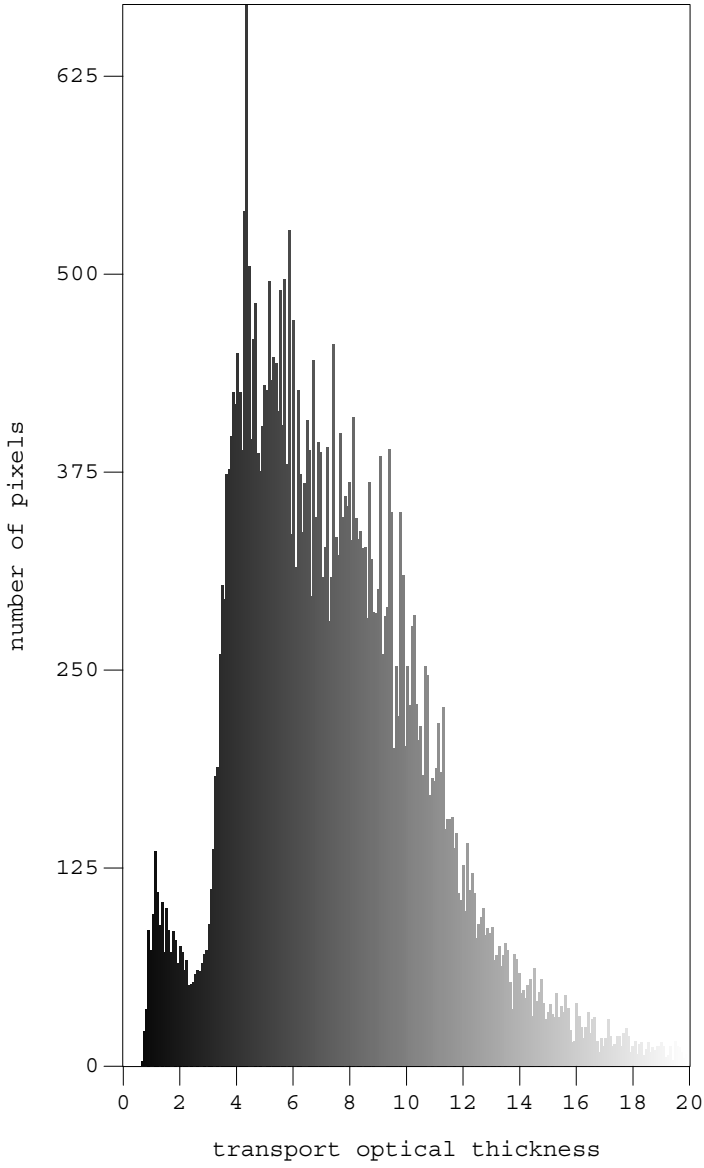

Fig. 4.20. The transport optical thickness frequency distribution.

4.2.2.3 The influence of ground albedo

The results of the cloud optical thickness retrievals are influenced by the ground reflectance. The ground reflectance is generally unknown. This may lead to considerable biases in retrievals. Sometimes minimal reflectance databases for a given

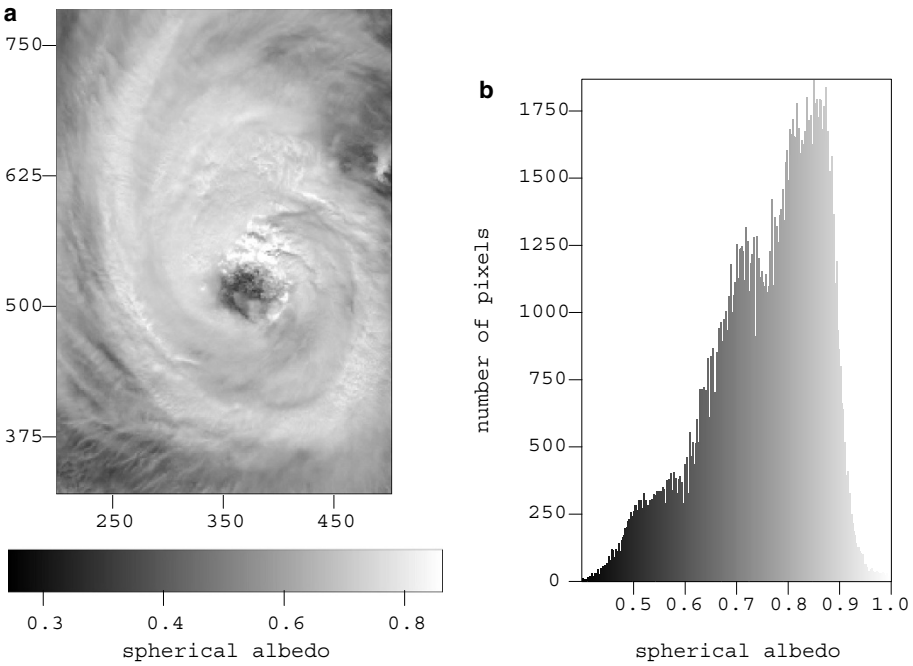

Fig. 4.21. The spherical albedo map (a) and the the spherical albedo frequency distribution (b).

location/month obtained from spaceborne observations for clear sky conditions are used to constrain the ground spectral reflectance.

It is of importance to understand in which conditions the influence of the ground reflectance can be neglected. Taking into account that the calibration error of modern spectrometers and radiometers is around 5%, we pose the following question. What is the Lambertian ground reflectance $A_{\max}$, which lead to not more than 5% differences between the cloud reflectances for a given $\tau = \tau'$ over black and not black underlying surfaces? Clearly, we can neglect the influence of the ground reflectance at $A < A_{\max}$ for a given cloud optical thickness $\tau = \tau'$.

This corresponds to the following equation:

$$1 - \frac{R_b}{R_A} = p, \tag{4.44}$$

where $p = 0.05$, R_b is the reflection function of a cloud over a black surface and R_A is the reflection function of a cloud over the ground surface having the albedo $A = A_{\max.}$ This equation can be rewritten in the following form for the Lambertian ground surface:

$$\frac{A_{\max} t^2 u_0(\mu) u_0(\mu)}{(1 - A_{\max}(1-t))\,(R_{0\infty} - t u_0(\mu) u_0\,(\mu_0))} = \frac{1-p}{p}, \tag{4.45}$$

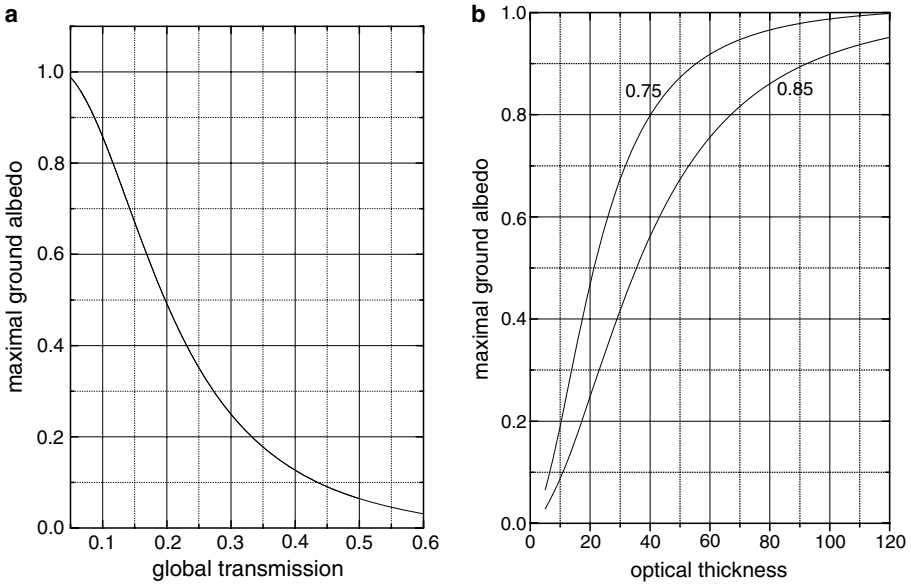

Fig. 4.22. (a) The dependence of the maximal ground albedo on the cloud transmission. (b) The dependence of the maximal ground albedo on the cloud optical thickness at $g = 0.75, 0.85$.

where we used Eq. (4.40a). So we have:

$$A_{\max} = \frac{\gamma \{Q - t\}}{\gamma (1 - t) \{Q - t\} + t^2}, \tag{4.46}$$

where $\gamma = p/(1 - p)$, $Q = R_{0\infty}(\eta, \xi, \varphi) / u_0(\eta) u_0(\xi)$. This equation allows to estimate the maximal value of the ground albedo, which can be neglected for a given p, t, and geometry. This can be easily generalized to account for the case $\omega_0 \neq 1$. Then values of $A_{\max}$ increase for a given τ.

The dependence of $A_{\max}$ on t is shown in Fig. 4.22a. It follows that for clouds having $t < 0.1$, the ground reflectance is of no importance for the geometry specified. We also show the dependence of $A_{\max}$ on cloud optical thickness in Fig. 4.22b at $g = 0.75$ (ice clouds), 0.85 (water clouds). Clearly, larger values of g lead to smaller cloud transmittances and, therefore, to smaller values of $A_{\max}$ for a given τ. This is supported by data shown in Fig. 4.22b as well. So we conclude that the account for ground reflectance is more important for water clouds as compared to ice clouds at a given τ. However, ice clouds are generally thinner as compared to water clouds and $A_{\max}$ decreases for smaller τ. So generally, surface effects cannot be neglected for ice clouds as well.

The snow ground reflectance in the visible is around 0.8. Then the ground albedo can be neglected for cloud optical thickness retrievals over snow at $\tau > \tau'$,

where $\tau' = 40$ for water clouds at $\tau' = 67$ for the geometry as specified in Fig. 4.22b. The value of τ' is around 5–10 for clouds over the ocean, where the ground albedo is small (generally, below 0.05 in the visible).

4.2.3 The Size of Droplets and Crystals

As was specified above, for a correct estimation of optical thickness of clouds from space, we need to know not only the surface albedo but also the effective radius of droplets. The size of droplets can be found if the reflection function in the near-infrared is measured simultaneously (Nakajima and King, 1990). This is due to the fact that the reflection function in the infrared strongly depends on the probability of photon absorption by droplets. This probability is proportional to the effective radius of droplets, as was discussed above.

The influence of absorption and scattering of light by molecules and aerosol particles on the measured value $R(\mu, \mu_0, \varphi, \tau)$ is often neglected in the cloud retrieval algorithms. However, correction can be easily taken into account if needed (Goloub et al., 2000; Wang and King, 1997). The influence of surface reflection on the cloud reflection function, assuming that the surface is Lambertian with albedo r, is easily taken into account, leading to following results (Kokhanovsky et al., 2003):

$$\hat{R}_1\left(a_{ef}, w\right) = R_{0\infty} - \frac{t_1\left(a_{ef}, w\right)\left[1 - A_1\right]}{1 - A_1\left[1 - t_1\left(a_{ef}, w\right)\right]} u_0(\xi) u_0(\eta), \tag{4.47a}$$

$$\begin{aligned}\hat{R}_2\left(a_{ef}, w\right) = {} & R_{0\infty} \exp\left(-y\left(a_{ef}\right)\left(1 - cy\left(a_{ef}\right)\right) u\right) \\ & - \left[\exp\left(-x\left(a_{ef}, w\right) - y\left(a_{ef}\right)\right) - \frac{t_2\left(a_{ef}, w\right) A_2}{1 - A_2 r_2\left(a_{ef}, w\right)}\right] \\ & \times t_2\left(a_{ef}, w\right) u_0(\xi) u_0(\eta).\end{aligned} \tag{4.47b}$$

The subscripts '1' and '2' refer to wavelengths λ_1 and λ_2 in the visible and the near-infrared channels respectively. The values of A_1 and A_2 give us the surface albedos in the visible and the near-infrared. The explicit dependence of functions involved on the parameters a_{ef} and w to be retrieved is introduced in brackets. The LWP w is preferred to the optical thickness in retrieval procedures due to the independence of w on wavelength. The optical thickness is uniquely defined if a_{ef} and w are known.

Equations 4.47a and (4.47b) form a nonlinear system of two algebraic equations having two unknowns (a_{ef} and w), which can be solved by standard methods and programs. In particular, we can find the value of w from Eq. (4.47a) analytically

(Kokhanovsky et al., 2003). Substitution of this result in Eq. (4.47b) gives us a single transcendent equation for the effective radius of droplets determination. The accuracy of this semi-analytical retrieval algorithm has been studied by Kokhanovsky et al. (2003).

A similar approach can be used for the estimation of sizes of crystals in ice clouds. The simplification is possible in this case. Due to the large size of crystals one can ignore the dependence of the reflectance in the visible on the size of particles and assume that $g \approx 3/4$ (Garrett et al., 2001; Kokhanovsky, 2004a). Then it follows assuming that $A_1 = 0$:

$$R = R_{0\infty} - \frac{u_0(\xi)u_0(\eta)}{1.072 + 0.188\tau}. \tag{4.48}$$

This equation allows for a simple estimation of τ in the case of thick ice clouds over black underlying surface. The functions $u_0(\xi)$ and $R_{0\infty}$ can be found from Eqs. (3.267) and (3.256), respectively. Knowing the value of τ and also accounting for the spectral neutrality of τ for ice clouds, we can obtain the cloud SSA. The size of particles can be derived from the value of SSA assuming the shape of ice crystals. Instead of the derivation of a crystal size for a given shape model, one can retrieve the particle absorption length as discussed by Kokhanovsky and Nauss (2005).

Usually the surface albedo is not known in advance and must be assessed using a priori assumptions or measurements over the same place but at a different time, when clear conditions prevail.

4.2.4 Single Scattering Albedo

Single scattering albedo measurements in infrared are easy and can be performed using LUT approach. Also the retrieved values of a_{ef} can be used to estimate the value of SSA. The problem is much harder in the visible, where the value of SSA is close to one. For polluted clouds the SSA is associated with pollutants (e.g., soot) and not with cloud droplets. Measurements in the infrared can be used to find both a_{ef} and τ enabling the calculation of the reflectance in the visible. This calculated value of the reflection function can be compared to the measured one to quantify the load of pollutants. However, it is not easy to estimate $\beta = 1 - \omega_0 \to 0$ from reflectance measurements due to calibration problems and also model assumptions used in retrieval procedures (e.g., cloud homogeneity). Generally, cloud absorptance can be measured using two aircrafts flying below and above a cloud and measuring transmittance and reflectance. Then the difference between incident and transmitted/reflected fluxes can be used to estimate the cloud absorptance a. However, the value of a is close to zero. Therefore, large errors in the retrieved value are possible.

King (1981) proposed to use just one aircraft but flying deep inside a cloud far from the boundaries. The aircraft must have instruments to measure downward and upward light fluxes or light filed intensities $i(\pm\eta)$. Then one can derive for an infinite cloud as $\beta \to 0 : D = i(-1)/i(1) = 1 - \zeta\sqrt{\beta}$, where $\zeta = 2\sqrt{3/(1-g)}$ as it was shown above. Therefore, it follows: $\beta = (1-D)^2/\zeta^2$ as $\beta \to 0$.

One must account for the influence of cloud boundaries. Then we have for the downward propagated light intensity (van de Hulst, 1968):

$$I(\eta) \sim i(\eta) - Wi(-\eta), \tag{4.49}$$

where the second term accounts for the influence of the boundary. Clearly, it follows: $W \to 0$ with τ_B, τ_B is the optical distance from the boundary to the level of measurements. Van de Hulst (1968) found that $W = \exp(-2k(\tau_B + q))$, where $q \approx 0.71/(1-g)$. So we have for the ratio $\tilde{D} = I(-1)/I(1)$:

$$\tilde{D} = \frac{i(-1) - Wi(1)}{i(1) - Wi(-1)}, \tag{4.50}$$

where we assume that the aircraft flies exactly in the middle of cloud and $\tau_B = \tau_0/2$, where τ_0 is the cloud optical thickness. Clearly, it follows for an infinite cloud: $\tau_0 \to \infty$ and $\tilde{D} \to D$. Also we can write:

$$\tilde{D} = \frac{D - W}{1 - DW}. \tag{4.51}$$

This equation allows to find the value of β, if $\tilde{D}$ is measured. For this, however, independent measurements of the cloud asymmetry parameter g are needed (Garrett et al., 2001). The analytical approximate expression for D valid at arbitrary β has been proposed by King (1986):

$$D = \frac{(1 - \sigma s)(1 - s)}{1 + \rho s}, \tag{4.52}$$

where $\sigma = 0.979$, $\rho = 1.503$, $s = \sqrt{(1-\omega_0)/(1-\omega_0 g)}$.

4.2.5 Cloud Thermodynamic Phase

The discrimination of liquid water from ice clouds is of importance for many applications, including flight safety and Earth climate studies. The size and shape of particles in warm and ice clouds are different. This influences the energy transmitted and reflected by a cloud.

This discrimination can be performed, taking into account the difference in angular or spectral distribution of reflected light. Also one can use polarization measurements as discussed by Goloub et al. (2000). It is known that minima in

the reflection function of ice clouds (e.g., near 1.5 and 2.0 μm) are moved to larger wavelengths as compared to the case of liquid droplets. This is, of course, due to the difference in spectral behaviour of the imaginary parts of the complex refractive index of liquid water and ice. Minima for liquid water also moved to larger wavelengths as compared to the absorption bands of water vapour. These different positions of minima can easily be registered with modern spectrometers (see, e.g., Dvoryashin, 2002; Knap et al., 2002).

Another possibility is to consider different angular behaviour of the reflection function for ice and water clouds at specific scattering geometries (e.g., rainbow, glory and halo scattering). In particular, the reflection function of water clouds, as distinct from ice clouds, has a maximum near the rainbow scattering angle, which also can easily be detected. This feature becomes even more pronounced if the degree of polarization [e.g., at the rainbow geometry] is studied (Goloub et al., 2000; Kokhanovsky, 2003b).

Yet another important problem is the detection of supercooled water in clouds. Kokhanovsky et al. (2006) proposed to use the P-T diagram for this purpose. Here P is the phase index equal to the ratio of the top-of-atmosphere reflectance at 1550 to that at 1670nm, T is the cloud top height temperature. The values of T above 273K correspond to water clouds. Then the values of P are above 0.8. However, it follows from the analysis of satellite data that in some cases T is below 273K at $P > 0.8$. These are areas, where supercooled water may exist. This issue is of importance for aircraft acing and safety.

4.2.6 Cloud Top Height and Cloud Fraction

Another important characteristic of a cloud is its height. It can be retrieved using data from space-borne lidars (Winker and Trepte, 1998). Passive measurements can also be used. For instance, Yamomoto and Wark (1961) proposed the use of the oxygen A band, centred at 0.761 μm. The physical basis of this method depends on a deep minimum around 0.761 μm due to oxygen absorption. The depth of the absorption band will depend on the cloud height. Photons can hardly penetrate thick clouds and be absorbed by the oxygen in the air column below the cloud. This will increase the value of the reflection function at 0.761 μm for the case of clouds at high altitudes. The depth of the absorption band is larger for low clouds. Practical applications of the method, however, are not so simple (Koelemeijer et al., 2001; Kuze and Chance, 1994; Rozanov and Kokhanovsky, 2004). First of all, the depth of band also depends on the oxygen absorption cross-section, which varies with temperature and pressure. Thus, one should use *a priori* assumptions on the temperature and pressure variation with height in the Earth's atmosphere. The generally unknown surface albedo and cloud geometrical thickness

influence the retrieval accuracy. Other possible sources of errors are described in detail by Kuze and Chance (1994) and Koelemeijer et al. (2001).

The largest complication arises for pixels that are only partially covered by clouds. Ignoring them will lead to a big reduction of data, so to overcome this problem Koelemeijer et al. (2001) proposed an algorithm that retrieves simultaneously effective cloud top height/pressure and cloud fraction, assuming that a cloud is a Lambertian surface with a given albedo. Such an assumption leads to underestimation of cloud top heights as compared to *in situ* measurements.

Rozanov and Kokhanovsky (2004) proposed the usage of the modified exponential approximation in the cloud top height retrievals. This allows to speed up the retrieval process considerably.

Global information on cloud fraction/cover $\mathbb{Q}$ is of a considerable importance by itself. Usually the value of $\mathbb{Q}$ varies in the range 0.55–0.85, depending on the exact region under study. Globally, clouds cover around 60% of the atmosphere. This once more underlines the importance of clouds in the radiation balance and atmosphere heating rates studies.

Palle and Butler (2001) state that the global cloud cover increased during the past century. They argue against a dominating role of solar activity (via galactic cosmic rays) on cloud formation.

4.2.7 Cloud Bottom Height

The cloud bottom height is usually determined using ground-based laser measurements. However, one can also assess the cloud bottom altitude from satellite measurements, if the cloud top altitude is known (e.g., from space lidar measurements). Let us show this considering a single homogeneous cloud. The cloud reflectance spectrum is hardly sensitive to the cloud geometrical characteristics outside gaseous absorption bands. The situation is radically changed if we consider the radiative transfer in the molecular absorption line (Rozanov and Kokhanovsky, 2004; Rozanov et al., 2004; Yamomoto and Wark, 1961). Indeed, let us assume that we have a gas in a planetary atmosphere, which absorbs almost all incident radiation in a narrow band. Then the depth of this band, measured by a receiver on a satellite will depend on the cloud altitude. Gas concentrations generally decrease with the distance from the ground. Therefore, clouds at a high altitude do not allow most photons to penetrate to low atmospheric layers and be absorbed there. So the depth of a molecular band in the reflected light will decrease, if high clouds are present in the field of view of a sensor. The next question to address is the influence of cloud geometrical thickness on the reflectance spectrum $R(\lambda)$ in the gaseous absorption band. One expects that spectra $R(\lambda)$ in the gaseous absorption band for clouds having the same top heights but different cloud geometrical thick-

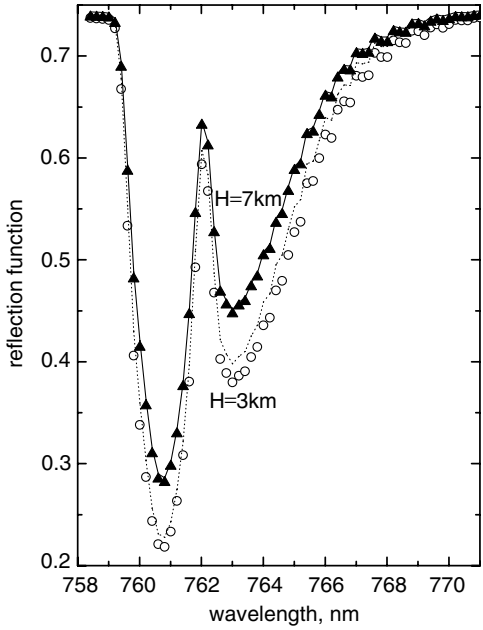

Fig. 4.23. Cloud reflection function in the oxygen A-band calculated using SCIATRAN (lines) (Rozanov et al., 2005) and asymptotic analytical theory (symbols) (Kokhanovsky and Rozanov, 2004) at the nadir observation, the solar zenith angle equal to 60°, the optical thickness equal to 50, the cloud top height equal to 9 km and cloud bottom height equal to 3 km (circles) and 7 km (triangles). All other parameters needed to calculations (e.g., atmospheric vertical profiles) coincide with those described by Kokhanovsky and Rozanov (2004). The reflectance function is averaged with the step 0.2 nm using SCIAMACHY (Bovensmann et al., 1999) response function.

nesses will differ even if the cloud optical thicknesses τ coincide (Kokhanovsky and Rozanov, 2004). This is due to the fact that multiple light scattering will lead to large average photon path lengths in clouds as compared to a cloudless atmosphere, thereby increasing absorption. This must lead to a decrease of the reflectance for geometrically thicker clouds. Radiative transfer calculations confirm this fact.

The dependence of the spectrum $R(\lambda)$ as shown in Fig. 4.23 can be used to determine the cloud bottom height from a satellite. The main steps of the inversion technique are given below.

Fist of all the TOA reflectance R is presented in the form of a Taylor expansion around the assumed value of the cloud bottom height equal to H_0:

$$R(H) = R(H_0) + \sum_{i=1}^{\infty} a_i (H - H_0)^i, \tag{4.53}$$

where $a_i = R^{(i)}(H_0)/i!$. Here $R^{(i)}(H_0)$ is the i-derivative of R at the point H_0. The next step is the linearization, which is a standard technique in the inversion procedures (Rozanov et al., 1998). We found that the function $R(H)$ is close to a linear one in a broad interval of the argument change (Kokhanovsky and Rozanov, 2004). Therefore, we neglect nonlinear terms in Eq. (4.53). Then it follows:

$$R = R(H_0) + R'(H_0)(H - H_0), \tag{4.54}$$

where $R' = dR/dH$. We assume that R is measured at several wavelengths $(\lambda_1, \lambda_2, \ldots \lambda_n)$ in the oxygen A-band. Then instead of the scalar quantity R we can introduce the vector $\vec{R}_{mes}$ with components $(R(\lambda_1), R(\lambda_2), \ldots R(\lambda_n))$. The same applies to other scalars in Eq. (4.53).

Therefore, Eq. (4.54) can be written in the following vector form:

$$\vec{y} = \vec{a}x \tag{4.55}$$

where $\vec{y} = \vec{R}_{mes} - \vec{R}(H_0)$, $\vec{a} = \vec{R}'(H_0)$ and $x = H - H_0$. Note that both measurement and model errors are contained in Eq. (4.55). The solution $\hat{x}$ of the inverse problem is obtained by minimizing the following cost function:

$$\Phi = \|\vec{y} - \vec{a}x\|^2, \tag{4.56}$$

where $\| \ \|$ means the norm in the Euclid space of the correspondent dimension.

The value of $\hat{x}$, where the function Φ has a minimum can be presented as

$$\hat{x} = \frac{(\vec{y}, \vec{a})}{(\vec{a}, \vec{a})} = \frac{\sum_{i=1}^{n} a_i y_i}{\sum_{i=1}^{n} a_i^2}, \tag{4.57}$$

where $(\vec{y}, \vec{a})$ denotes a scalar product in the Euclid space, and n is the number of wavelengths where the reflection function is measured.

The functions $\vec{R}(H_0)$ and $\vec{R}'(H_0)$ in Eq. (4.57) must be calculated using the radiative transfer theory with input parameters characteristic for a given atmospheric state. We use the approximate analytical theory for such a calculation. The details of this theory are given by Kokhanovsky and Rozanov (2004). Basically, the approximation has an accuracy better than 5% as compared to line-by-line calculations in the O_2 A-band (Kokhanovsky and Rozanov, 2004) for typical cloudiness with $\tau \geq 5$. The use of the exact radiative transfer theory is also possible but it leads to a huge calculation time and does not provide a better approach to the problem at hand due to all uncertainties involved (e.g., possible multi-layered cloudiness).

Therefore, knowing values of the measured spectral reflection function R_{mes} and also values of the calculated reflection function R and its derivative R' at $H = H_0$ and several wavelengths, the value of the cloud bottom height can be found from Eq. (4.57) and equality: $H = \hat{x} + H_0$. The value of H_0 can be taken

equal to 0.5 km, which is a typical value for low level clouds. The main assumption in our derivation is that the dependence of R on H can be presented by a linear function on the interval x (Kokhanovsky and Rozanov, 2004).

The retrieved value of H is compared to H_0. If the difference is smaller than 100 m, the value of H is taken as a retrieved value and the inversion procedure is finished. Otherwise, the retrieved value of H is substituted in Eq. (4.56) instead of H_0 and iterations are performed until the convergence is reached.

Several additional parameters are needed in the retrieval procedure. They are the cloud optical thickness, the cloud liquid water profile, the cloud droplet radii, etc. They must be simultaneously derived or assumed using climatological values. We have found that the cloud optical thickness τ is the most important parameter which influences the retrieval. So we find the value of τ from measurements outside the gaseous absorption band as described by Kokhanovsky and von Hoyningen-Huene (2004).

Clearly, if the forward and inverse models use the same system of equations, the inverse problem solution accurately reproduces the input parameters for the forward model in the absence of the measurement noise. We have checked this using the forward and inverse models based on the same set of analytical equations as described by Rozanov and Kokhanovsky (2004). Indeed, the cloud bottom height used as input in the retrieval scheme coincided with the cloud bottom height retrieved by the solution of the inverse problem as specified above in this case.

The next possible step is to introduce measurement errors and see the influence of these errors on the retrieval of H. However, we have chosen a different strategy. Namely, we calculate the cloud reflectance spectrum $R(\lambda)$ in the O_2 A-band using the exact radiative transfer calculations with the radiative transfer solver SCIATRAN (Rozanov et al., 2005) and use this exact spectrum in the analytical retrieval procedure described above. Because possible measurement errors are well below the accuracy of analytical equations, such an approach can be considered as a simulation of noise in the inversion procedure having as an input SCIATRAN-generated synthetic spectra.

Results of the inversion procedure described above are shown in Fig. 4.24. It follows that with the exclusion of clouds having large top altitude and small cloud bottom height (very thick clouds), which are rare cases in terrestrial atmosphere, there is a one-to-one correspondence between retrieved H_r and exact H_e cloud bottom heights. Biases $\Delta H = H_r - H_e$ are given in Fig. 4.25. It follows that biases are only weakly influenced by values of τ and generally they are below 0.5 km for clouds having the geometrical thickness below 4.5 km. Most clouds in the terrestrial atmosphere have geometrical thicknesses below 1 km. Then biases are just 0.25 km as shown in Fig. 4.25.

Therefore, we conclude that the technique presented here can be used for an accurate estimation of a cloud bottom height from a satellite.

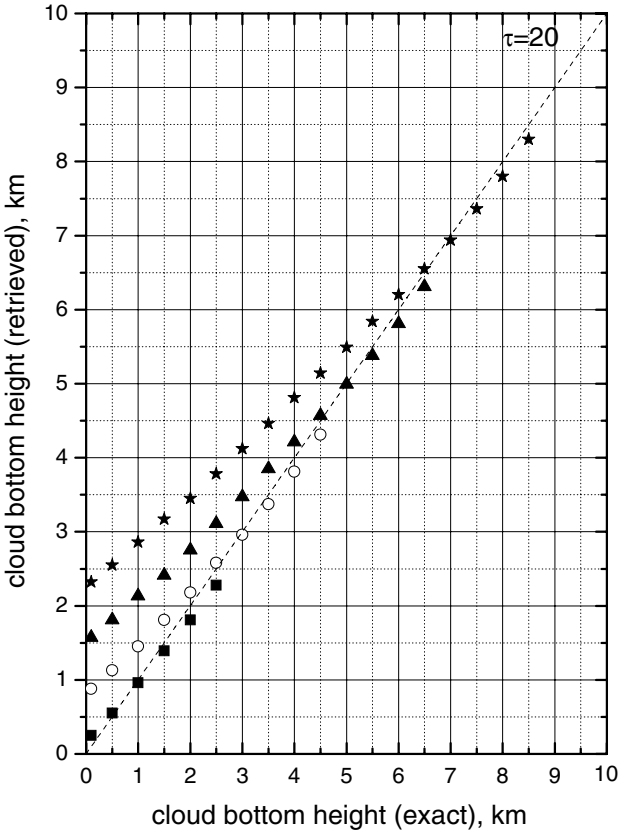

Fig. 4.24. Dependence of the retrieved cloud bottom height on the exact cloud bottom height at $\tau = 20$ for cloud top height 9 km (stars), 7 km (triangles), 5 km (circles), 3 km (squares).

It follows from Fig. 4.25 that the accuracy of the retrieval decreases for smaller values of H. This is related to the fact that analytical equations have large errors for smaller H. Note that the probability of single clouds having small values of H and large values of the cloud top height is low. So values with large biases of the retrieved cloud bottom altitude as shown in Fig. 4.25 do not produce significant biases as far as the operational cloud retrievals are concerned.

The results given in Figs. 4.24 and 4.25 are obtained allowing for the cloud top height measurements uncertainty $\Delta h = \pm 10$ m. They are not changed appreciably even when increasing this uncertainty $10\times$ (e.g., to 100 m). The changes of biases as shown in Fig. 4.25 are generally below 30 m then. It means that the considered technique can be easily implemented using the lidar system. Lidars can detect the cloud boundary with the accuracy better than 20 m.

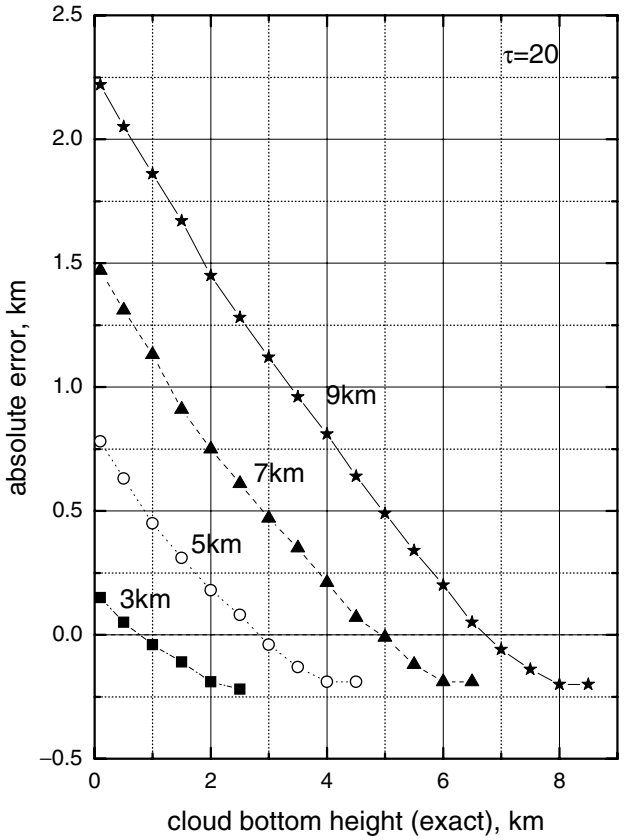

Fig. 4.25. Dependence of the absolute error of the retrieved cloud bottom height on the exact cloud bottom height at $\tau = 20$ for cloud top height 9 km (stars), 7 km (triangles), 5 km (circles), 3 km (squares). Data are obtained from Fig. 4.24.

4.3 Laser Beam Propagation Through a Cloud

The studies of laser beam propagation through fogs and clouds are of importance for a number of applied problems including sounding of clouds and also for image transfer, vision and communication problems. The aim of this section is to derive the angular distribution of a light field inside a cloud under laser beam illumination conditions along a normal to a cloud or fog layer (e.g., along axis *OZ*). Unlike most problems considered above, we need to account for the horizontal inhomogeneity of a multiply scattered light field. This inhomogeneity arises solely due to boundary conditions. A laser beam enters a cloud effectively at one point. So instead of

uniform illumination of the cloud boundary, we have illumination of a cloud by a narrow beam. The intensity of light at a given depth depends not only on the observation direction but also on the distance of a given point from the axis *OZ*, which gives the illumination direction. For simplicity of derivations we will assume that a cloud is represented by a homogeneous layer. Theory is easily extended for a case of vertically inhomogeneous cloudy media.

The main equation of the problem can be written in the following form:

$$(\vec{s}\vec{\nabla})I(\vec{r},\vec{s}) + \sigma_{ext}I(\vec{r},\vec{s}) - \frac{\sigma_{sca}}{4\pi}\int_{4\pi} I(\vec{r},\vec{s}')p(\vec{s}',\vec{s})d\Omega' = 0. \tag{4.58}$$

The task is to find the angular distribution of light field $I(\vec{r},\vec{s})$ at a given point $\vec{r}$ in the direction specified by the vector $\vec{s}$ assuming a narrow beam illumination condition. Generally, the problem looks complicated and calls for the numerical implementation. However, an important approximate solution can be derived, if one is interested in the distribution $I(\vec{r},\vec{s})$ close to the axis of the laser beam for vectors $\vec{s}$ directed along *OZ* or in the directions almost parallel to *OZ*. Let us show this.

We present vectors $\vec{r}$ and $\vec{s}$ as

$$\vec{r} = x\vec{e}_x + y\vec{e}_y + z\vec{e}_z, \tag{4.59}$$

$$\vec{s} = s_x\vec{e}_x + s_y\vec{e}_y + s_z\vec{e}_z, \tag{4.60}$$

where $(\vec{e}_x,\vec{e}_y,\vec{e}_z)$ are unity vectors directed along the axes *OX, OY,* and *OZ*. Axes *OX* and *OY* specify the plane perpendicular to *OZ*. We can write in the spherical coordinate system:

$$s_x = \sin\theta\cos\varphi,\ \ s_y = \sin\theta\sin\varphi,\ \ s_z = \cos\theta. \tag{4.61}$$

Here φ is the azimuthal angle and θ is the angle between the axis *OZ* and the observation direction. We will assume that $\theta \to 0$ in our derivations. Hence, the correspondent approximation is called the small angle approximation (SAA). Clearly, this is the generalization of the SAA considered above for a case of narrow beams.

Let us introduce the vector

$$\vec{\nabla}_\perp \equiv \vec{e}_x\frac{\partial}{\partial x} + \vec{e}_y\frac{\partial}{\partial y}. \tag{4.62}$$

Then it follows

$$(\vec{s}\vec{\nabla}_\perp)I(z,\vec{\rho},\vec{s}) + \frac{\partial I(z,\vec{\rho},\vec{s})}{\partial z} + \sigma_{ext}I(z,\vec{\rho},\vec{s}) - \frac{\sigma_{sca}}{4\pi}\int_{-\infty}^{\infty} ds_x'\int_{-\infty}^{\infty} ds_y' I(z,\vec{\rho},\vec{s}')p(\vec{s}-\vec{s}') = 0, \tag{4.63}$$

Table 4.1. Fourier transforms.

N	Fourier transform	Definition
1	$\tilde{I}(z,\vec{\nu},\vec{s})$	$\int_{-\infty}^{\infty}\int_{-\infty}^{\infty} I(z,\vec{\rho},\vec{s})e^{i\vec{\nu}\vec{\rho}}d\vec{\rho}$
2	$I(z,\vec{\rho},\vec{s})$	$\frac{1}{4\pi^2}\int_{-\infty}^{\infty}\int_{-\infty}^{\infty}\tilde{I}(z,\vec{\nu},\vec{s})e^{-i\vec{\nu}\vec{\rho}}d\vec{s}$
3	$-i\vec{s}\vec{\nu}\tilde{I}(z,\vec{\nu},\vec{s})$	$\int_{-\infty}^{\infty}\int_{-\infty}^{\infty}(\vec{s}\vec{\nabla}_{\perp})I(z,\vec{\rho},\vec{s})e^{i\vec{\nu}\vec{\rho}}d\vec{\rho}$
4	$\tilde{p}(\vec{q})$	$\int_{-\infty}^{\infty}\int_{-\infty}^{\infty} p(\vec{s})e^{i\vec{q}\vec{s}}d\vec{s}$
5	$\tilde{h}(\vec{\nu})=\tilde{f}(\vec{\nu})\tilde{g}(\vec{\nu})$	$h(\vec{\beta})=\int_{-\infty}^{\infty}\int_{-\infty}^{\infty} f(\vec{\alpha})g(\vec{\beta}-\vec{\alpha})d\vec{\alpha}$
6	$\tilde{\tilde{G}}(z,\vec{\nu},\vec{q})$	$\int_{-\infty}^{\infty}\int_{-\infty}^{\infty} p(\vec{s})e^{i(\vec{q}-z\vec{\nu})\vec{s}}d\vec{s}$
7	$\tilde{D}(z,\vec{\nu},\vec{s})$	$\frac{1}{4\pi^2}\int_{-\infty}^{\infty}\int_{-\infty}^{\infty}\tilde{\tilde{D}}(z,\vec{\nu},\vec{q})e^{-i\vec{q}\vec{s}}d\vec{q}$
8	1	$\int_{-\infty}^{\infty}\int_{-\infty}^{\infty}\delta(\vec{s})e^{-i\vec{\nu}\vec{s}}d\vec{s}$

where we used the fact that $ds_x ds_y = \cos\theta\sin\theta d\theta d\varphi = \cos\theta d\Omega \approx d\Omega$ and $s_z \approx 1$ as $\theta \to 0$. Also we assume that the phase function depends only on the difference vector $\vec{d} = \vec{s} - \vec{s}'$ and introduce the transverse vector $\vec{\rho} = x\vec{e}_x + y\vec{e}_y$. We use infinite limits of integration because the contribution of photons located at large distances from the axis OZ is low. Clearly, our assumptions are valid only if light scattering occurs predominantly in the forward direction and this is really the case for fogs and clouds due to highly extended phase functions for these cases. The approximation considered is not valid in deep layers of a cloud (e.g., at $\tau \geq 5$) because then light deviates from the axis OZ considerably.

Equation (4.63) can be solved analytically. We show this using the Fourier transform technique. Applying the Fourier transform with respect to $\vec{\rho}$ to Eq. (4.63), we have using definitions specified in Table 4.1:

$$\hat{\Lambda}\tilde{I}(z,\vec{\nu},\vec{s}) - \frac{\sigma_{sca}}{4\pi}\int_{-\infty}^{\infty}\int_{-\infty}^{\infty} d\vec{s}'\tilde{I}(z,\vec{\nu},\vec{s}')p(\vec{s}-\vec{s}') = 0, \tag{4.64}$$

where $\hat{\Lambda} \equiv (\partial/\partial z) + \sigma_{ext} - i\vec{s}\vec{\nu}$. This equation can be simplified using the substitution:

$$\tilde{I}(z,\vec{\nu},\vec{s}) = \tilde{D}(z,\vec{\nu},\vec{s})\exp(iz\vec{\nu}\vec{s} - \tau), \tag{4.65}$$

where $\tau = \sigma_{ext}\, z$. Then it follows:

$$\frac{d\tilde{D}(z, \vec{\nu}, \vec{s})}{dz} - \frac{\sigma_{sca}}{4\pi} \int_{-\infty}^{\infty} \int_{-\infty}^{\infty} \tilde{D}(z, \vec{\nu}, \vec{s}\,')\tilde{G}(z, \vec{\nu}, \vec{s} - \vec{s}\,')d\vec{s}\,' = 0, \tag{4.66}$$

where

$$\tilde{G}(\vec{s} - \vec{s}\,') = p(\vec{s} - \vec{s}\,') \exp(i\vec{\nu}z(\vec{s} - \vec{s}\,')). \tag{4.67}$$

Let us apply the Fourier transform with respect to $\vec{s}$ to Eq. (4.66). The integral in Eq. (4.66) can be transformed using the convolution property 5 in Table 4.1. Then it follows:

$$\frac{d\tilde{\tilde{D}}(z, \vec{\nu}, \vec{q})}{dz} - \frac{\sigma_{sca}}{4\pi} \tilde{\tilde{D}}(z, \vec{\nu}, \vec{q})\tilde{\tilde{G}}(z, \vec{\nu}, \vec{q}) = 0. \tag{4.68}$$

$\tilde{\tilde{D}}_{\mathrm{i}}$ the double Fourier transform of D (with respect to both $\vec{\rho}$ and $\vec{s}$). The expression for $\tilde{\tilde{G}}$ is given in Table 4.1. Comparing lines 1 and 5 in Table 4.1, we derive: $\tilde{\tilde{G}} \equiv \tilde{p}(\vec{q} - \vec{\nu}z)$. Therefore, it follows from Eq. (4.68):

$$\tilde{\tilde{D}}(z, \vec{\nu}, \vec{q}) = A \exp\left\{ \frac{\sigma_{sca}}{4\pi} \int_0^z \tilde{p}\,(\vec{q} - \vec{\nu}z)\, dz \right\}, \tag{4.69}$$

where $A \equiv \tilde{\tilde{D}}(0, \vec{\nu}, \vec{q})$ is the integration constant. This solves the problem at hand. Indeed, the value of $\tilde{D}(z, \vec{\nu}, \vec{s})$ in Eq. (4.65) can be found using the inverse Fourier transform as specified in Table 4.1 (line 7). Then it follows for the angular distribution of light at point $\vec{\rho}$ in the direction $\vec{s}$ (see line 2 in Table 4.1):

$$I(z, \vec{\rho}, \vec{s}) = \frac{1}{4\pi^2} \int_{-\infty}^{\infty} \int_{-\infty}^{\infty} \tilde{I}(z, \vec{\nu}, \vec{s})e^{-i\vec{\nu}\vec{\rho}}d\vec{\nu}, \tag{4.70}$$

where

$$\tilde{I}(z, \vec{\nu}, \vec{s}) = \frac{1}{4\pi^2} \int_{-\infty}^{\infty} \int_{-\infty}^{\infty} \tilde{D}(z, \vec{\nu}, \vec{q}) \exp(-i\vec{s}\vec{q} + i\vec{s}\vec{\nu}z - \tau)d\vec{q}. \tag{4.71}$$

Although the numerical integration is required to find $I(z, \vec{\rho}, \vec{s})$, a number of important results can be obtained in numerous special cases as considered by Ishimaru (1978).

Note that Eq. (4.70) can be rewritten in yet another form:

$$I(z, \vec{\rho}, \vec{s}) = \left(\frac{1}{2\pi}\right)^4 \int_{-\infty}^{\infty} \int_{-\infty}^{\infty} \int_{-\infty}^{\infty} \int_{-\infty}^{\infty} \tilde{\tilde{I}}(z, \vec{\nu}, \vec{q})e^{-i(\vec{\nu}\rho + \vec{q}\vec{s})}d\vec{\nu}d\vec{q}, \tag{4.72}$$

where

$$\tilde{\tilde{I}}(z,\vec{\nu},\vec{q}) = H(\vec{\nu},\vec{q}+\vec{\nu}z)\exp\left\{-\sigma_{sca}z + \frac{\sigma_{sca}}{4\pi}\int_0^z \tilde{p}(\vec{q}-\vec{\nu}(z'-z))dz'\right\} \tag{4.73}$$

and $H(\vec{\nu},\vec{\kappa})$ is determined from boundary conditions:

$$H(\vec{\nu},\vec{\kappa}) = \int_{-\infty}^{\infty}\int_{-\infty}^{\infty}\int_{-\infty}^{\infty}\int_{-\infty}^{\infty} d\vec{\rho}d\vec{s}\,I(0,\vec{\rho},\vec{s}). \tag{4.74}$$

Equation (4.73) plays an important role in Fourier optics of light scattering media. In particular, assuming that $I(0,\vec{\rho},\vec{s}) = \delta(\vec{\rho})\delta(\vec{s})$ and using property 8 in Table 4.1, we derive:

$$\tilde{\tilde{I}}(z,\vec{\nu},\vec{q}) = \exp\left\{-\sigma_{sca}z + \frac{\sigma_{sca}}{4\pi}\int_0^z \tilde{p}(\vec{q}-\vec{\nu}(z'-z))dz'\right\}. \tag{4.75}$$

Calculations of $\tilde{p}$ can be simplified assuming the circular symmetry of the phase function: $p(\vec{s}) \equiv p(|\vec{s}_\perp|) = p(s)$. Then it follows:

$$\tilde{p}(\kappa) = 2\pi\int_0^\infty p(s)J_0(\kappa s)sds. \tag{4.76}$$

Therefore, we can write:

$$\tilde{\tilde{I}}(z,\vec{\nu},\vec{q}) = \exp\left\{-\sigma_{sca}z + \frac{\sigma_{sca}}{2}\int_0^z dz'\int_0^\infty d\theta p(\theta)J_0((q-\nu z')\theta)\theta\right\}. \tag{4.77}$$

It follows from this equation at $\vec{\nu} = \vec{q} = \vec{0}$:

$$\tilde{\tilde{I}}(z,\vec{0},\vec{0}) = \exp\left\{-\sigma_{sca}z + \frac{\sigma_{sca}}{2}\int_0^z dz'\int_0^\infty d\theta p(\theta)\theta\right\} \tag{4.78}$$

or $\tilde{\tilde{I}}(z,\vec{0},\vec{0}) = 1$, where we accounted for the phase function normalization condition:

$$\frac{1}{2}\int_0^\infty p(\theta)\theta d\theta = 1. \tag{4.79}$$

The SAA as considered here can be generalized for the inclined incident beams with the incidence angle $\vartheta_0 \neq 0$. It can be also used to study laser backscattering in a simple approximation based on the consideration of small angle scattering in the forward direction, one single scattering backwards and the SAA in the backward

direction [the quasi-single approximation (QSA)]. Details are given by Katsev et al. (1998). Note that the QSA considerably improves theoretical considerations of laser backscattering by cloudy media as compared to the traditionally used lidar equation:

$$I = Cz^{-2}\sigma_{sca}(z)\exp\left\{-2\int_0^z \sigma_{ext}(z')dz'\right\}. \tag{4.80}$$

Here C is the lidar constant dependent on the transmitted power, pulse duration and receiver characteristics. The value of $\sigma_{sca}(z)$ gives the backscattering coefficient at the range z.

4.4 Image Transfer Through Clouds and Fogs

From the point of view of the linear systems theory a cloud is a high frequency filter. The transmission of high frequency signals (in time and space domains) is reduced considerably in comparison with low frequency signals as a result of light scattering. We introduce here the main concepts of the Fourier optics of clouds.

Any diffused source of light can be considered as a superposition of point light sources. Thus, in linear optical systems the image of such an object with the irradiance $a_0(\vec{r}')$ is a linear superposition of images of point sources. This can be represented as

$$a(\vec{r}) = \int_{-\infty}^{\infty}\int_{-\infty}^{\infty} S(\vec{r},\vec{r}')a_0(\vec{r}')d\vec{r}', \tag{4.81}$$

where the point spread function (PSF) $S(\vec{r}',\vec{r})$ describes the process of the transformation of the object irradiance $a_0(\vec{r}')$ in the initial plane to the image irradiance $a(\vec{r})$ in the image plane. The PSF is a main notion of the image transfer theory (ITT). Equation (4.81) takes a simpler form in the frequency domain:

$$a(\vec{\upsilon}) = S(\vec{\upsilon})a_0(\vec{\upsilon}), \tag{4.82}$$

where

$$a(\vec{\upsilon}) = \int_{-\infty}^{\infty}\int_{-\infty}^{\infty} a(\vec{r}')e^{-i\vec{\upsilon}\vec{r}'}d\vec{r}', \tag{4.83}$$

$$a_0(\vec{\upsilon}) = \int_{-\infty}^{\infty}\int_{-\infty}^{\infty} a_0(\vec{r}')e^{-i\vec{\upsilon}\vec{r}'}d\vec{r}', \tag{4.84}$$

$$S(\vec{\upsilon}) = \int_{-\infty}^{\infty}\int_{-\infty}^{\infty} S\left(\vec{r}'\right)e^{-i\vec{\upsilon}\vec{r}'}d\vec{r}', \tag{4.85}$$

and $\vec{\upsilon}$ is the space frequency. We see that the integration procedures in the Fourier space can be substituted by the multiplication. This makes all calculations much simpler.

One of the basic problems of the ITT is to determine the Fourier transform of the PSF, namely the optical transfer function (OTF) $S(\vec{\upsilon})$ or the modulation transfer function

$$T(\vec{\upsilon}) = \frac{|S(\vec{\upsilon})|}{|S(0)|}. \tag{4.86}$$

Also we have then:

$$a(\vec{r}') = \frac{1}{4\pi^2} \int_{-\infty}^{\infty} \int_{-\infty}^{\infty} a(\vec{\upsilon}) e^{i\vec{\upsilon}\vec{r}} d\vec{\upsilon}. \tag{4.87}$$

The OTF depends on the properties of media between an object and an image (Wells, 1969; Ishimaru, 1978; Volnistova and Drofa, 1986; Zege et al., 1991). Let us consider the case of fogs and cloudy media in the visible range. Then particles are large as compared to the wavelength and the SAA as described above can be used to solve the problem. We will study the image transfer along axis *OZ* perpendicular to a cloud layer. In this case the OTF is a real function. It does not depend on the azimuth for randomly oriented particles.

The SAA for the OTF follows from Eq. (4.77) at $\vec{q} = 0$. Namely, we have:

$$\tilde{\tilde{I}}(z, \nu, 0) = \exp\left\{-\sigma_{sca} z + \frac{\sigma_{sca}}{2} \int_0^z dz' \int_0^{\infty} d\theta p(\theta) J_0\left(\nu z' \theta\right) \theta\right\}. \tag{4.88}$$

It can be proved that $\tilde{\tilde{I}}(z, \nu, 0) \equiv S(z, \nu)$. Indeed, the double Fourier transform of the intensity $I(z, \vec{\rho}, \vec{s})$ has the following form:

$$I(z, \vec{\nu}, \vec{q}) = \int_{-\infty}^{\infty} \int_{-\infty}^{\infty} \int_{-\infty}^{\infty} \int_{-\infty}^{\infty} I(z, \vec{\rho}, \vec{s}) e^{i(\vec{\nu}\vec{\rho} + \vec{q}\vec{s})} d\vec{\nu} d\vec{s}. \tag{4.89}$$

So we have at $\vec{q} = 0$:

$$I(z, \vec{\nu}, 0) = \int_{-\infty}^{\infty} \int_{-\infty}^{\infty} a(z, \vec{\rho}) e^{i\vec{\nu}\vec{\rho}} d\vec{\nu}, \tag{4.90}$$

where

$$a(z, \vec{\rho}) = \int_{-\infty}^{\infty} \int_{-\infty}^{\infty} I(z, \vec{\rho}, \vec{s}) d\vec{s}. \tag{4.91}$$

Comparing Eqs. (4.28) and (4.33), we conclude that $S(z, \vec{\nu}) \equiv I(z, \vec{\nu}, 0)$. So we have:

$$S(z, \nu) = \exp\left\{-\tau\left\{1 - \omega_0 B(\nu, z)\right\}\right\}, \tag{4.92}$$

where

$$B(\nu, z) = \frac{1}{2z} \int_0^z dz' \tilde{p}(\nu(z - z')). \tag{4.93}$$

Let us introduce a new variable $\varsigma = 1 - z'/z$. Then it follows:

$$B(\nu, z) = \frac{1}{2} \int_0^1 d\varsigma \tilde{p}(\nu z \varsigma). \tag{4.94}$$

We see that $B(\nu, z)$ depends on the dimensionless frequency $\kappa = \nu z$. The same is true for the OTF. Therefore, it follows:

$$S(\kappa) = \exp\{-\tau\{1 - \omega_0 B(\kappa)\}\}, \tag{4.95}$$

where

$$B(\kappa) = \frac{1}{2} \int_0^1 \tilde{p}(\kappa \varsigma) d\varsigma. \tag{4.96}$$

Equation (4.95) is of a great importance in the Fourier optics of clouds. This equation allows to derive the irradiance in the image plane if one knows the irradiance in the initial plane using Eq. (4.82). Also it follows:

$$a_0(\kappa) = S^{-1}(\kappa) a(\kappa). \tag{4.97}$$

Therefore, the initial image can be reconstructed, if the OTF is known.

It follows at $\kappa = 0$: $S(\kappa) = \exp(-\sigma_{abs} z)$. Therefore, only absorption processes are responsible for the OTF reduction at the zero frequency.

Let us approximate the phase function of a cloud medium as

$$p(\theta) = 4\alpha^2 \exp(-\alpha^2 \theta^2). \tag{4.98}$$

Then it follows:

$$\tilde{p}(\varsigma\kappa) = \exp\left\{-\frac{\varsigma^2 \kappa^2}{4\alpha^2}\right\} \tag{4.99}$$

and, therefore:

$$B(\kappa) = \frac{\alpha\sqrt{\pi}}{\kappa} erf\left[\frac{\kappa}{2\alpha}\right], \tag{4.100}$$

where the error function

$$erf(u) = \frac{2}{\sqrt{\pi}} \int_0^u \exp(-\phi^2) d\phi \tag{4.101}$$

is introduced. So we obtain the following analytical expression for the OTF:

$$S(\kappa) = \exp\left\{-\tau\left\{1 - \frac{\alpha\omega_0\sqrt{\pi}}{\kappa} erf\left[\frac{\kappa}{2\alpha}\right]\right\}\right\}. \tag{4.102}$$

In particular, it follows as $\kappa \to 0$:

$$erf\left[\frac{\kappa}{2\alpha}\right] \approx \frac{\kappa}{\alpha\sqrt{\pi}}\left[1 - \frac{\kappa^2}{12\alpha^2}\right] \tag{4.103}$$

and, therefore,

$$S(\kappa) = \exp\left\{-\tau\left[1 - \omega_0\left(1 - \frac{\kappa^2}{12\alpha^2}\right)\right]\right\}. \tag{4.104}$$

It follows for non-absorbing media: $S(\kappa) = \exp\{-\Xi\kappa^2\}$, where $\Xi = \tau/12\alpha^2$. We see that the distribution $S(\kappa)$ has the Gaussain shape at small dimensionless frequencies κ. Larger droplets in clouds are characterized by more extended phase functions. Therefore, α must be larger for larger particles. This also means that the OTF is larger for larger particles. This will lead to a better image quality for media having larger particles. Further details on the image transfer are given by Ishimaru (1978) and Zege et al. (1991).

In conclusion, let us consider the case $\vec{\nu} = 0$ in the general expression. Then it follows:

$$\tilde{\tilde{I}}(z, 0, q) = \exp\left\{-\sigma_{sca} z + \frac{\sigma_{sca} z}{2}\int_0^\infty d\theta p(\theta) J_0(q\theta)\theta\right\} \tag{4.105}$$

or

$$\tilde{\tilde{I}}(z, 0, q) = \exp\{-\sigma_{sca} z(1 - \tilde{p}(q)\}, \tag{4.106}$$

where

$$\tilde{p}(q) = \frac{1}{2}\int_0^\infty p(\theta) J_0(q\theta)\theta d\theta. \tag{4.107}$$

Using Eq. (4.32), we obtain:

$$I(z, 0, \vec{s}) = \int_{-\infty}^{\infty}\int_{-\infty}^{\infty} I(z, \vec{s}) e^{i\vec{q}\vec{s}} d\vec{s}, \tag{4.108}$$

where

$$I(z, \vec{s}) = \int_{-\infty}^{\infty}\int_{-\infty}^{\infty} I(z, \vec{\rho}, \vec{s}) d\vec{\rho}. \tag{4.109}$$

$\tilde{\tilde{I}}(z, 0, q)$ gives the angular spectrum of transmitted light. According to Zege et al. (1991), this function coincides with the mutual coherence function (MCF) $\Gamma(z, q)$:

$$\Gamma(z, q) = \exp\{-\sigma_{sca} z(1 - \tilde{p}(q))\}. \tag{4.110}$$

So one can study also the coherence loss due to scattering processes in cloudy media using approximate results presented here. By definition, the inverse Fourier transform of $\Gamma(z, q)$ gives the angular distribution of light transmitted through a scattering layer having the geometrical thickness z. Further discussions of this topic are given by Zege and Kokhanovsky (1994).

4.5 Clouds and Climate

The weather could be highly variable at any given place. However, meteorological characteristics (e.g., surface temperature T_s) are quite stable if one considers their average values for long periods of time (e.g., month, year, 100 years). The climate is the averaged weather. It is argued that the human activity leads to the climate change on a global scale. For instance, there is a strong correlation between the increase of the surface temperature T_s and the increase of the concentration c of CO_2 in the atmosphere. It is believed that c increases due to human activity and this leads to the increase of T_s. There are also other human factors, which influence the climate (in particular, the extensive land use and industrial production). All this constitutes a major scientific problem of modern time, namely, the climate change and its influence on the biosphere. Another issue is how we may change human behaviour to minimize its possibly disastrous influence on climate (e.g., melting of ice at northern latitudes). Clouds influence climate in many ways. First of all they reflect a large portion of incident solar energy back to outer space cooling the system. So the change of cloud albedo, which is influenced by cloud optical thickness and in a smaller extent by cloud thermodynamic state and size of particles is very important. Clouds also warm the system protecting the escape of energy from our planet at night. This is especially true for high clouds. Therefore, we see that not only the cloud thicknesses but also their altitudes are of importance for climate studies. Polluted clouds (e.g., containing soot) also warm the Earth-atmosphere system reflecting less solar energy back to outer space. However, pollution can also lead to larger droplet concentrations and, therefore, to smaller particles. This leads to the increase of reflectance by cloudy media.

The energy balance equation can be written in the following form:

$$(1 - r)\frac{E_0}{4} = \sigma T^4, \tag{4.111}$$

where r is the global average albedo, σ is the Stefan–Botzman constant, E_0 is the solar constant and T_{ef} is averaged radiation temperature. The coefficient 1/4 shows that the illuminated surface (πa^2) is 4 times smaller than the emission surface

($4\pi a^2$). Here a is the radius of Earth. Basically, this equation means that energy transmitted through the top-of-atmosphere escapes to outer space through thermal radiative effects. This equation is only approximately valid because it ignores many important processes. However, Eq. (4.111) clearly shows that the temperature T_{ef} is influenced mainly by the albedo of the planet r:

$$T_{ef} = \sqrt[4]{\frac{1-r}{4\sigma}E_0}. \tag{4.112}$$

In turn, the albedo of the planet is mainly determined by its cloud cover and cloud thickness. This simple example shows the importance of clouds in the climate problem. Note that the surface temperature T_s averaged on large time intervals (e.g., 1 year) is highly correlated with the product $x = \sigma T_{ef}^4$. In particular, it was found that (in °C): $T_s = 0.5\sigma T_{ef}^4 - 104$. Using values $E_0 = 1360\frac{W}{m^2}$, $r = 0.3$, we obtain that 1% increase in r will result in the cooling of the surface by approximately 0.5°C.

Therefore, it is of great importance to monitor the albedo of cloudless atmosphere and also clouds on a global scale.

Such observations make a substantial contribution to the most important scientific problem of modern time—studies of climate change.